

Clemson University

TigerPrints

Publications

Automotive Engineering

6-2022

Numerical Implementation and Validation of a Viscoelastic-Plastic Material Model for Predicting Curing Induced Residual Stresses in Adhesive Bonded Joints

Akshat Agha

Fadi Abu-Farha

Follow this and additional works at: https://tigerprints.clemson.edu/auto_eng_pub



Part of the [Automotive Engineering Commons](#), and the [Materials Science and Engineering Commons](#)

Numerical Implementation and Validation of a Viscoelastic-Plastic Material Model for Predicting Curing Induced Residual Stresses in Adhesive Bonded Joints

Akshat Agha*¹, Fadi Abu-Farha¹

¹*Clemson University - International Center for Automotive Research, Greenville, SC, USA*

** Corresponding Author. Tel +1 (336) 346 4213; E-mail: aagha@clmson.edu*

DOI: <https://doi.org/10.1016/j.ijadhadh.2022.103195>

Published in International Journal of Adhesion and Adhesives

ABSTRACT

One of the main challenges in the joining of multi-material components is the assessment of the nature and magnitude of the residual stresses developing in the adhesive bond during the heat curing manufacturing process. Numerical modeling of these residual stresses can provide insights for making informed decisions related to (i) material substrate properties; (ii) adhesive properties i.e. low, medium, or high stiffness; (iii) bondline geometry i.e. bondline width and bead thickness; (iv) curing cycle characteristics; and (v) fixation design i.e. type, spacing, the number of joints. This work presents a cure history-dependent viscoelastic-plastic material description for the modeling of adhesive bonded joints. The main highlight of the work is the multi-physics modeling package consisting of a curing kinetics model, a cure-dependent viscoelastic model, and a temperature, strain-rate dependent plastic model formulation which can be coded in any finite element solver. The modeling approach can predict the residual stresses in the adhesive bond due to the accumulated viscoelastic as well as plastic strains occurring during the heat curing process. For the purpose of validation, the model is coded into a user-defined material subroutine (UMAT) in LS-DYNA. The modeling approach is verified at a small specimen level by simulating a uniaxial tension specimen at various temperatures and strain rates. The performance of the modeling approach is further evaluated at the component level using specially designed experiments involving heat curing of a sub-sized multi-material automotive roof model. The thermal displacements and distortions in the roof structure captured using 3D digital image correlation are compared to the finite element model predictions. Several design guidelines related to adhesive selection and mechanical fixations are proposed as a result of the study.

KEYWORDS

Curing, adhesive, material modeling, multi-material joint, residual stress, viscoelastic, plastic, user-defined material subroutine, UMAT

1. INTRODUCTION

1.1. Background

In recent times, the automotive industry has seen a huge shift from steel-intensive body-in-white (BIW) to highly complex multi-material lightweight structures making use of modern materials. The introduction and mixing of new materials (like advanced high strength steels, aluminum alloys, magnesium alloys, and fiber-reinforced composites) to create a single component has led to the development of new manufacturing processes and joining techniques, as the conventionally popular joining techniques like spot welding fail to perform [1] for multi-material joints. In this scenario, adhesive bonding is a viable method for joining dissimilar materials; it enables high-performance and flexible joints while eliminating the weight and cost of mechanical fasteners. However, adhesive bonding has its limitations. Automotive-grade structural adhesives are heat-cured epoxy-based thermosets. The heat curing process poses a critical problem pertaining to the differences in the coefficient of thermal expansion (CTE) of the joined materials; the mismatch of which has significant implications on the integrity and response of the BIW to external loading (mainly thermal).

Due to the ease of manufacturing, and economic reasons, adhesive curing is combined with the automotive paint baking process. Figure 1 presents the phenomenon happening inside the paint baking oven. At an elevated temperature in the paint baking oven, the multi-material parts of an adhesively joined component expand at different rates and magnitudes depending on their different CTE and temperature gradient due to varying air convection properties. The uncured adhesive (in the form of a compliant viscoelastic liquid) does not pose any restriction to the thermal displacements in the substrates. However, the adhesive gets fully cured and attains its stiffness at a high temperature when the joined substrates are in a thermally expanded state. Due to this, the fully cured adhesive poses restriction to the substrate movement during the thermal contraction in the components during the cooling down phase. This (when extended to all components and different joints in a BIW) leads to distortion in the body structure, and more importantly harmful residual stresses in the adhesive-bonded joints. It is well established that the presence of such residual stresses is detrimental to the performance of the adhesive bond and thereby of the automobile body structure during the service life of the vehicle, particularly in case of a crash event as shown by Reddy et al. [2] and Akshat et al. [3].

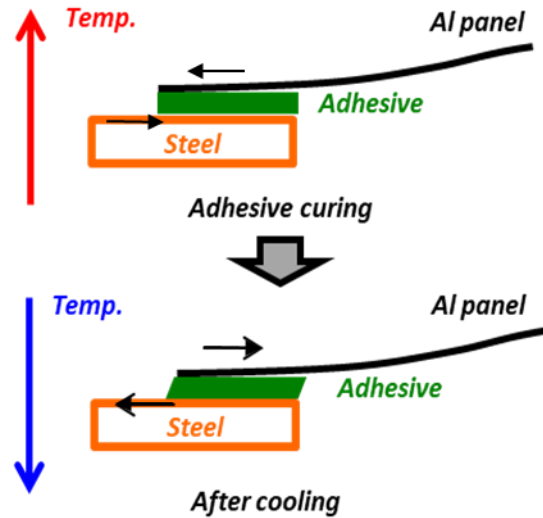


Figure 1. Pictorial representation of the problem due to the thermal expansion and contraction in substrates during the heat curing process of an adhesive bonded joint

It is crucial to understand the nature and magnitude of the curing-induced residual stresses and quantify the structural distortions to optimize the design and manufacturing process. Due to the absence of any direct and reliable technique for measuring the residual stresses in the adhesive bond [4], it is important to predict them using analytical or numerical approaches. Several works in the literature have attempted to model the residual stresses in the epoxy resins, especially epoxy-based carbon fiber composites to study the delamination behavior. The simplest approach is to model the residual stresses assuming the epoxy resin to be fully elastic, as done by Xiaogang [5] and Brauner [6]. An improvement to this approach was suggested by Ruiz et al. [7], and Li et al. [8] who used viscoelastic models to model the epoxy behavior. Notable work has been done by Adolf and Martin [9], Prasatya et al. [10], Courtois et al. [11] to model the cure-dependent viscoelastic behavior of toughened epoxy resins. It is established in the literature by da Silva et al. [12] that fully cured automotive grade adhesives exhibit plastic behavior in addition to the viscoelastic behavior. Another work by Budhe et al. [13] suggests that the adhesives show viscoelastic behavior during curing and some plastic behavior after getting fully cured.

In a previous work, Akshat et al. [14] presented a suite of models to predict the manufacturing process-induced residual stresses in the heat-cured thermoset adhesives using viscoelastic formulation dependent on the degree of cure and temperature. A simplistic yet effective method to evaluate the effects of the heat curing process on the adhesive-bonded joint was discussed, but the viscoelastic modeling approach can be further improved by accounting for the plastic behavior of the adhesive.

Just like metals, the adhesives show rate dependency and temperature-dependent plastic properties [15, 16]. It is also seen that the yield strength of the adhesive is also temperature dependent, and it drops with increase in temperature. The main significance of the plastic model lies in the cooling down phase of the adhesive bond in the paint baking cycle. At the start of the cooling phase, when the adhesive is fully cured, it begins to show viscoelastic-plastic behavior. At this stage, the viscoelastic modulus and the yield strength of the adhesive are low due to the high temperature. As the temperature decreases with time, the viscoelastic modulus and the yield strength increase together. At any stage, if the effective stress in

the adhesive bond, caused due to thermal contraction in the substrates, becomes higher than the yield strength of the adhesive, the adhesive accumulates plastic strains. Considering this, it is necessary to model the plastic component of the adhesive to accurately model the curing induced effects on the adhesive bond.

This paper attempts to bridge that gap and provides a cure-dependent, temperature-dependent, and rate-dependent viscoelastic-plastic approach for modeling the adhesive bond during manufacturing (heat curing) and carrying over the manufacturing induced effects in the post-manufacturing (service life) phase of the component.

1.2. Framework of the study

The adhesive bonding process contains many aspects of material behavior occurring simultaneously and interacting with each other. A successful numerical modeling approach needs to adequately describe all the aspects of the 'multi-physics' nature of the problem. The employed modeling approach is, therefore, divided into three components: (i) Curing Kinetics model to calculate the degree of cure of the adhesive based on the time and temperature history; (ii) Degree of cure and temperature-dependent viscoelastic model to calculate the viscoelastic stresses during the heat curing process; (iii) Temperature and strain-rate dependent viscoelastic-plastic model to calculate the residual stresses in the fully cured adhesive during the heat curing process and the service life of the adhesive bond. The three models are integrated and are coded into a user-defined material subroutine (UMAT) for LS-DYNA.

The next section introduces the theory behind the proposed material models. Section 3 presents the experiments performed for model calibration. Section 4 discusses the mathematical formulation behind the user-defined material subroutine (UMAT). In section 5, the developed material subroutine is validated against experiments performed at the component level using a small-scale automotive roof component.

2. MATERIAL MODELING

Different parts of the BIW experience different time-temperature histories as they are heated inside a paint baking oven (owing to their different thermal properties, local air convection characteristics, design intricacy, and location in the structure) which directly affects the conditions for adhesive curing across the structure [17, 18]. The mechanical properties of an adhesive bond are dependent on the degree of cure of the adhesive. Therefore, it is crucial to accurately determine the degree of cure to accurately model the mechanical behavior of the adhesive during the curing and post-curing process. Then, we need a mechanical model which can predict the mechanical properties of the adhesive depending on the degree of cure and temperature.

The total strain in the adhesive is decomposed into the following strain components:

$$\varepsilon_{total} = \varepsilon_{elastic} + \varepsilon_{viscous} + \varepsilon_{plastic} + \varepsilon_{thermal} + \varepsilon_{shrinkage} \quad (1)$$

In a previous paper by Akshat [14], an approach was shown to model only the cure-dependent viscoelastic behavior of the adhesive. In this paper, the modeling approach is refined to include the plastic component of strain in the formulation.

It is also shown in several studies that the stresses generated due to chemical shrinkage and thermal expansion in the adhesive itself are relatively small and their relevance for automotive applications are

insignificant as compared to other phenomenon, like the CTE mismatch of substrates [4, 19]. In a pursuit to keep the modeling simple yet effective, the effect of chemical shrinkage and the thermal expansion/contraction in the adhesive itself have been skipped from the modeling approach.

Hence, this work is divided into three models, (i) Curing Kinetics model and (ii) Viscoelastic model (iii) Plastic model.

2.1. Curing Kinetics Model

The process of conversion of an adhesive from viscoelastic liquid state to a viscoelastic-plastic state in the presence of a catalyst is called as curing of adhesive. As discussed earlier, the automotive grade structural adhesives are heat cured adhesives, which need to be exposed to elevated temperatures for curing. When a thermosetting epoxy is heated, it undergoes a chemical reaction and gets cured to form a three-dimensional cross-linked network which is irreversibly locked in place and can't be reformed or reprocessed. The degree of cure/conversion (represented as α) of an adhesive is a function of the temperature-time history that the adhesive is exposed to and is represented as a number ranging from 0 to 1. The rate of conversion with respect to time can be mathematically described as:

$$\frac{d\alpha}{dt} = f(\alpha) \cdot K(T) \quad (2)$$

where, $f(\alpha)$ is a phenomenological reaction model, while $K(T)$ is the temperature dependent function defined by an Arrhenius relationship, which is:

$$K(T) = A \exp(-E_a/RT) \quad (3)$$

where, A is the pre-exponential constant, E_a is the activation energy, R is the universal gas constant and T is the temperature. Several reaction models are published in the literature which can satisfactorily predict the reaction rate of polymers. After an extensive literature survey, the reaction model chosen for this work was Kamal's Model [20] which has been validated in several studies based on epoxy resins. The said model can be shown as:

$$f(\alpha) = (k_1 + k_2 \alpha^m)(1 - \alpha)^n \quad (4)$$

where, k_1 is the zero conversion rate value, k_2 is the auto-catalytic rate constant, m is the auto-catalytic exponent and n is the order of the reaction model.

2.2. Viscoelastic Model

Adhesives are known to show time and temperature dependent viscoelastic behavior. The viscoelastic properties of an adhesive depend on the degree of cure, so the modeling approach is divided into two sections: (1) Viscoelastic model for fully cured material, (2) Cure-dependent viscoelastic model.

2.2.1. Viscoelastic model for fully cured material

The time and temperature dependent properties of a thermorheologically simple linear viscoelastic material at an arbitrary temperature (within the range) can be estimated from the properties at a certain reference temperature by using time-temperature superposition principle. The modulus vs. frequency curve at the reference temperature is known as master curve, and the properties at a lower or higher

temperature can be obtained by shifting the master curve left or right on the log frequency axis. The discrete frequency shift factors for each temperature are recorded and fit to a continuous mathematical model, required for modeling. Owing to its versatility to a wide range of polymers, the shift factors were fitted to WLF shift function [21] which is given by:

$$\text{Log}(a_T) = -A' \frac{T - T_{REF}}{B' + T - T_{REF}} \quad (5)$$

where, a_T is the frequency shift factor for the current temperature T ; T_{REF} is the reference temperature at which the master curve was drawn, while A' and B' are curve fitting parameters.

The master curve which is a representation of the relaxation behavior of the viscoelastic material can be modeled by Generalized Maxwell Model [22, 23]. The Generalized Maxwell model is mathematically expressed by Prony series expansion:

$$G(t, \alpha) = G_0(\alpha) \left(1 - \sum_j \frac{G_{j, \alpha=1}}{G_{0, \alpha=1}} (1 - e^{-\beta_j t}) \right) \quad (6)$$

where, $G_0(\alpha)$ is the instantaneous shear modulus as a function of the degree of cure, j represents the number of terms in Prony series expansion, $G_{j, \alpha=1}$ is the shear relaxation modulus for the j^{th} term for the fully cured material and β_j is the shear decay constant for the j^{th} term for the fully cured material. The Generalized Maxwell Model equation can be expressed in terms of the instantaneous modulus G_0 or the long term (equilibrium) modulus G_∞ which are equivalent. It was presented in terms of G_0 here. As per Eq. (6), at time $t = 0$ the value of $G(t) = G_0$, while at time $t = \infty$ the value of $G(t)$ becomes G_∞ .

2.2.2. Cure-dependent viscoelastic model

The fundamental need in establishing cure dependence is to predict the instantaneous modulus at a certain cure level and an approximation of the relaxation behavior at that cure level. Several authors have discussed the phenomenon of gelification. A resin's gel point represents a certain degree of cure which is associated with the start of buildup of its mechanical properties. Several authors assumed that below the gelation point, the adhesive is so compliant that the modulus is negligible, and all the stresses are immediately relaxed [9, 11].

The popular approach used in modeling is to assume that the cure-dependent relaxation behavior (i.e. the relaxation time) is same as that of a fully cured system, with the effective shift factor as a multiplicative product of temperature shift and cure shift [11, 22, 23]. Kim and White [24] proposed an enhancement to Maxwell model by making instantaneous modulus, relaxation modulus and decay constants as a function of degree of cure. Another approach is to use phenomenological models like DiBenedetto equation which calculate the glass transition temperature based on the degree of cure and then use the glass transition temperature to predict the shift factors of the viscoelastic model. The approach used in this work is based on the work of Bogetti and Gillespie [25], who used a mathematical equation to determine the cure-dependent equilibrium modulus using the degree of cure and full cure equilibrium modulus. The dependency of the equilibrium modulus is approximated by using the following equation:

$$G_{\infty}(\alpha) = G_{\infty}(1) \left(\frac{\alpha^2 - \alpha_{gel}^2}{1 - \alpha_{gel}^2} \right)^{8/3} \quad (7)$$

where, $G_{\infty}(1)$ is the equilibrium modulus at full cure, α_{gel} is the cure level at the point of gelification and α is the cure level at which the modulus is to be determined. The evolution of G_0 with cure is considered to be the same as G_{∞} , i.e., G_0 grows from 0 at the point of gelification to its highest attained value at full cure in the same ratio as G_{∞} . For the sake of keeping the formulation simple, it is assumed that the relaxation behavior at the time of curing is like the relaxation of fully cured material i.e. the temperature dependent shift factors obtained for a fully cured adhesive will be used for modeling the partially cured adhesive. The consequences of this assumption will be evaluated in the experimental validation section of the paper.

2.3. Plastic Model

The plastic model defines the trend of the stress-strain curve of a material after the yield limit. For defining the temperature and rate dependent nature of adhesives, the plastic constitutive model in the current formulation should take into account the effects of temperature and strain rate. For this purpose, the flow stress is defined by the Johnson-Cook flow stress model [26] which is defined by the following equation:

$$\sigma = (A'' + B\varepsilon^n)(1 + C \text{Log}_{10} \dot{\varepsilon}^*)(1 - T^*)^m \quad (8)$$

$$T^* = (T - T_0)/(T_m - T_0) \quad (9)$$

$$\dot{\varepsilon}^* = \dot{\varepsilon}/\dot{\varepsilon}_{REF} \quad (10)$$

Where ε is the plastic strain, $\dot{\varepsilon}$ is the plastic strain rate, $\dot{\varepsilon}_{REF}$ is the reference quasi-static plastic strain rate, T_0 is the reference temperature, T_m is the reference melt temperature, and A'' , B , C , m , and n are material constants. The choice of the plastic model will be evaluated based on the fit of the experimental curves.

The modeling approach is based on two basic assumptions:

- (i) The cure-dependent behavior of the adhesive is modeled using the viscoelastic material description, and the adhesive behaves purely viscoelastic when it is partially cured (Degree of cure $\alpha < 0.9$).
- (ii) The temperature dependent plastic behavior of the adhesive is active only after attaining a fully cured state (Degree of cure $\alpha > 0.9$). The reason behind this assumption is that the viscoelastic stresses in the partially cured adhesive are significantly small and do not ever cross the plastic yield limit.

The next section of the paper discusses the experiments performed and the approach used in calibrating the above material models from the experimental data.

3. EXPERIMENTS AND MODEL CALIBRATION

The adhesive used in this work is an automotive-grade structural adhesive Henkel Teroson EP 5089. It is a single component epoxy-based thermosetting adhesive. Three sets of tests were run on the adhesive to calibrate the material models. They are Differential Scanning Calorimetry (DSC) to calibrate the curing kinetics model, Dynamic Mechanical Analysis (DMA) to calibrate the viscoelastic mechanical model, and uniaxial tension tests at high temperatures and varying strain rates to calibrate the plastic mechanical model.

3.1. Calibration of curing kinetics model

Adhesive curing is an exothermic process which means that energy is expelled when an adhesive is being cured. The energy released during curing of a thermosetting adhesive can be captured using DSC tests as shown in several studies. This is achieved by exposing the uncured adhesive specimen to a controlled temperature ramp and analyzing the characteristics of the resulting exothermic cure peak while the adhesive cures in the DSC. In this work, DSC measurements were performed using DSC Q20 model from TA Instruments. Prior to the test, a specified weight of Teroson EP 5089 adhesive was cooled in the machine from room temperature to -40°C for conditioning for at least 5 minutes. And then the DSC scans were run by heating the sample from -40°C to 250°C at constant heating rates of 0.5, 1, 2, 5, 10 and $20^{\circ}\text{C}/\text{min}$. DSC tests were also performed at isothermal conditions at 140°C and 160°C . A sample DSC map normalized with the adhesive weight for heating rates of 0.5, 1, 2 and $5^{\circ}\text{C}/\text{min}$ is shown in the appendix *Figure A.1*. The readers can download the DSC data for EP5089 in raw format from [27] for reproducing the work.

The DSC curves were numerically transformed to give the degree of cure vs. temperature and time curves as shown in the appendix *Figure A.2*. For a detailed explanation of the model fitting procedure, the readers can refer to previous publications by Akshat et al. [14, 28].

The fitting parameters for the curing kinetics model given in Eq. (2),(3) and (4) for EP 5089 are given in *Table 1*.

A (1/s)	E_a (kJ/mol)	k_1	k_2	m	n
$e^{22.06}$	99.72	0.26	5.16	1.15	1.46

Table 1. Calibrated parameters for curing kinetics model

The calibrated curing kinetics model was validated against the experimental curing curves for heating rates of 10 and $20^{\circ}\text{C}/\text{min}$ and isothermal tests at 140°C and 160°C . A comparison of the model estimation and experimental curves is shown in the appendix *Figure A.3 and A.4*.

3.2 Calibration of viscoelastic model

3.2.1. Fully cured material

Henkel Teroson EP 5089, being an epoxy-based adhesive shows viscoelastic properties. The viscoelastic properties dependent on temperature and frequency are measured using a dynamic mechanical analysis system (DMA). The output of the DMA tests are viscoelastic moduli (storage and loss modulus) measured at different frequencies and temperatures. According to the theory of viscoelasticity, the real part of the modulus – storage modulus G_s and the imaginary part of the modulus – loss modulus G_l combine to form

a complex modulus $G = G_S + iG_L$, where i is the imaginary unit number. The damping loss factor can be calculated by $\eta = \tan\delta = \frac{G_L}{G_S}$ where δ is the phase shift between real and imaginary part of modulus.

In this work, DMA measurements were performed with a bar in a torsional configuration. The DMA setup measures stress vs. strain curve which can be used to calculate complex moduli. The modulus was obtained for a fully cured specimen for a combined frequency and temperature sweep, with a 0.1% strain amplitude, for a frequency range of 0.1 Hz to 100 Hz at a temperature range of -50 °C to 200 °C at a step of 10 °C. The storage modulus as a result of combined temperature and frequency sweep from DMA tests is shown in the appendix *Figure A.5*. It is seen that with a rise in temperature, the material softens and the modulus decreases. The readers can download the DMA data for EP5089 in raw format from [29] for easy reproduction of the work.

Using time-temperature superposition principle applicable to linear viscoelastic materials, the modulus curves were shifted horizontally on the logarithmic frequency axis. For a reference temperature of 100 °C, the curves at higher temperature in the lower portion of the plot were shifted to the left (to lower frequencies) and the curves at lower temperature were shifted to the right (to higher frequencies), in order to generate a smooth continuous curve. The frequency shift factors were recorded for each temperature and were later fit to WLF shift function, given in Eq. (5). The shifted modulus curve (known as Master curve at 100 °C) was drawn for storage, loss modulus and loss factor, as shown in *Figure A.6*. The scatter in the loss modulus values at higher temperatures is a result of phase changes in the material due to the actual temperature going beyond the glass transition temperature of the full cured material.

The experimental master curve for EP 5089 at 100 °C and the shift factors were fit to the Generalized Maxwell model with 16 elements of Prony series expansion given in Eq. (6) and WLF Shift function given in Eq. (5), and the calibrated parameters are given in *Table 2*. A comparison of the experimental and estimated values is shown in *Figure A.6 and Figure A.7*. It suggests that the shift factor is negative for temperatures higher than 100 °C and positive for temperatures lower than 100 °C, which means higher temperatures shift to the left and lower temperatures shift to the right on the frequency axis. The estimations for loss modulus and loss factor are wavy, which is typical for Prony series expansion, but represent the general trend of the experimental values.

According to the Prony fitting results shown in *Table 2*, the instantaneous modulus (G_0) of the material is 1578 MPa, while the long-term modulus (G_∞) of the material is 6.63 MPa. This means that the material relaxes with time and after a long time ($\sim 1E6$ seconds) the modulus drops to 6.63 MPa.

The bulk modulus of the adhesive was calculated based on Poisson's ratio of 0.4 and the instantaneous shear modulus of 1578 MPa. The bulk modulus was taken to be independent of time and conversion, $K_\infty(\alpha) = K_0 = K_\infty = 7362$ MPa.

Parameters for Prony Series Expansion Eq. (6)					
	Shear Relaxation Modulus (G_j) [MPa]	Shear Decay Constant (β_j) [Hz]		Shear Relaxation Modulus (G_j) [MPa]	Shear Decay Constant (β_j) [Hz]
G1	119.02	1.00E+24	G9	109.05	1.00E+08
G2	143.49	1.00E+22	G10	133.60	1.00E+06
G3	153.10	1.00E+20	G11	134.42	1.00E+04

G4	126.43	1.00E+18	G12	129.81	1.00E+02
G5	131.26	1.00E+16	G13	88.92	1.00E+00
G6	102.49	1.00E+14	G14	15.59	1.00E-02
G7	91.12	1.00E+12	G15	0.93	1.00E-04
G8	91.79	1.00E+10	G16	0.01	1.00E-06
G_0	1578 MPa				
G_∞	6.63 MPa				
Parameters for WLF Frequency Shift Function Eq. (5)					
WLF A'	88				
WLF B'	751 K				
WLF T_{REF}	373 K				
Parameters for Cure-dependent Equilibrium Modulus Function Eq. (7)					
α_{gel}	0.56				

Table 2. Parameters obtained for best fit of WLF shift function and 16 elements of Prony series expansion

3.2.2. Cure-dependent viscoelastic model

To capture the curing dependency of the material, DMA tests were run on an uncured sample of the adhesive between two plates in torsional configuration at 0.3 rad/s oscillation with a 0.1% strain amplitude. The adhesive was allowed to cure in the DMA while two sets of tests were run with dynamic temperature ramps of 5°C/min and 10°C/min from room temperature to 180°C and 220°C respectively. The measurement results are shown in Figure A.8 and Figure A.9.

The test data shows that the modulus for the uncured adhesive was negligible in the beginning and as the temperature increased with time, the adhesive gets cured and the modulus picks up and reaches a steady value which is very close to the value of equilibrium modulus (6.63 MPa) previously calculated by Prony series for full cured adhesive, in section 3.2.1. The experimental results were transformed from modulus vs. time and temperature to modulus vs. cure using the curing kinetics model developed in section 3.1. The experimental results were fit to Eq. (7) and the best fitting for the data is obtained at $\alpha_{gel} = 0.56$ using the full cured equilibrium modulus value of 6.63 MPa. *Figure A.10* shows a comparison of the experimental results for modulus vs. cure along with the model estimation.

3.3 Calibration of plastic model

The plastic properties of the adhesive were studied by conducting tensile tests on fully cured adhesive specimens. A new methodology was developed to produce adhesive specimens by curing sheets of adhesive between two parallel steel plates. This ensured uniform thickness and the same curing conditions for every specimen. The steel-adhesive-steel sandwich for preparing an adhesive sheet was cured in a furnace at 180°C for 35 mins. The procedure is depicted schematically in *Figure 2*. The adhesive sheets were then put into a specially prepared die to shear the tensile dog bone specimens from them as depicted in *Figure 3*.

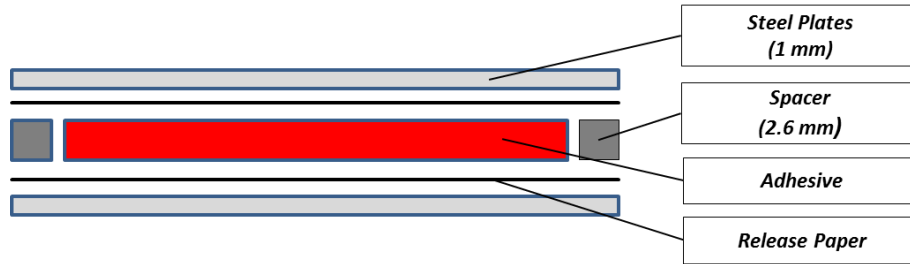


Figure 2. Adhesive sheet preparation – cured between two steel sheets

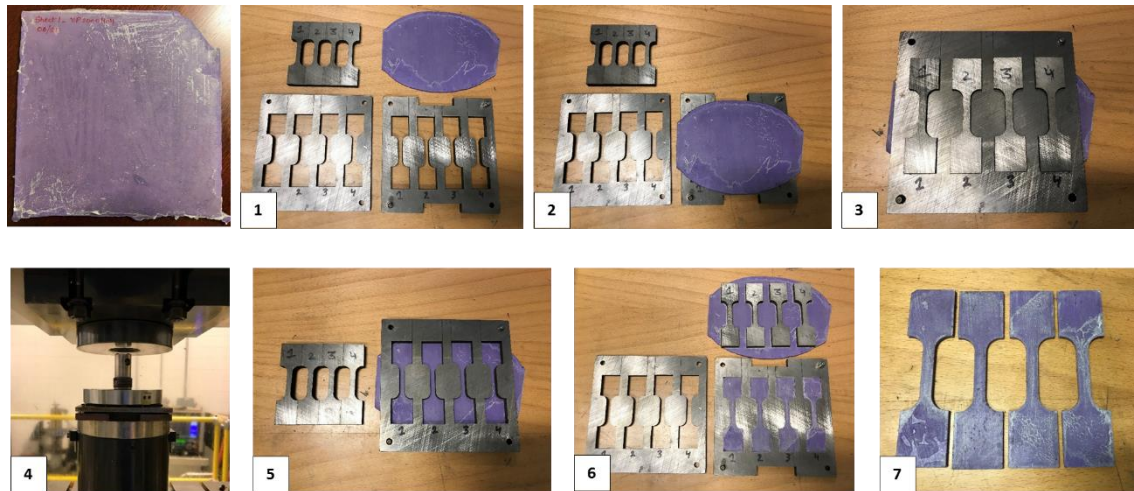


Figure 3. Tensile specimen preparation using specially prepared die

The adhesive specimens were pulled in tension on an Instron quasi-static electromechanical load frame with a 50kN load cell. The setup consisted of a furnace mounted on the load frame for conducting high-temperature tests. The furnace had a small glass window opening through which optical strain measurements were done using GOM ARAMIS 5-Megapixel 3D-DIC system. The test setup included specially designed grips for high-temperature testing, which allowed easy specimen loading/unloading and self-alignment of the specimen. The test setup is shown in Figure 4. The tests were performed at four temperatures (25°C, 60°C, 90°C, 120°C) and three strain rates (1E-3 /s, 1E-2 /s, 1E-1 /s). The tests at different strain rates were performed at room temperature, while the tests at different temperatures were performed at the quasi-static strain rate 1E-3 /s. The readers can refer to the high-temperature and high-strain rate tensile testing results for EP5089 from the public repository [30].

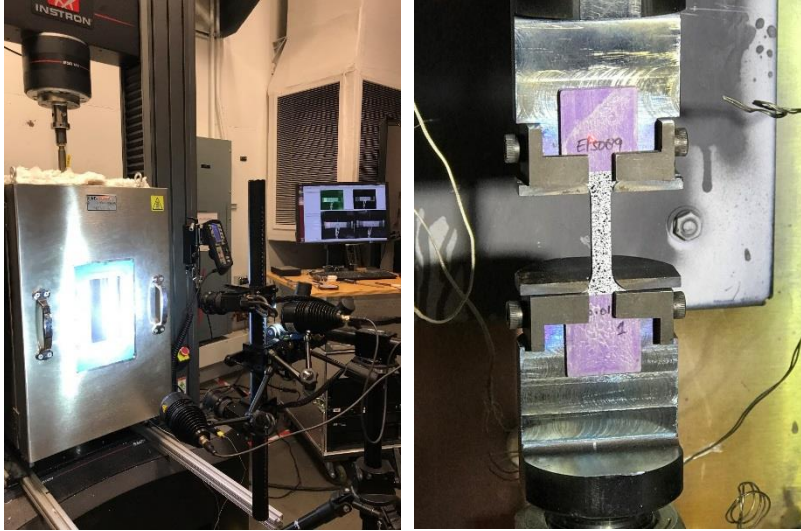


Figure 4. (a) Test setup showing furnace and 3D-DIC (b) Custom grips for high-temperature tensile testing on adhesive samples

The stress-strain curves obtained from the tests are shown in Figure 5 and Figure 6.

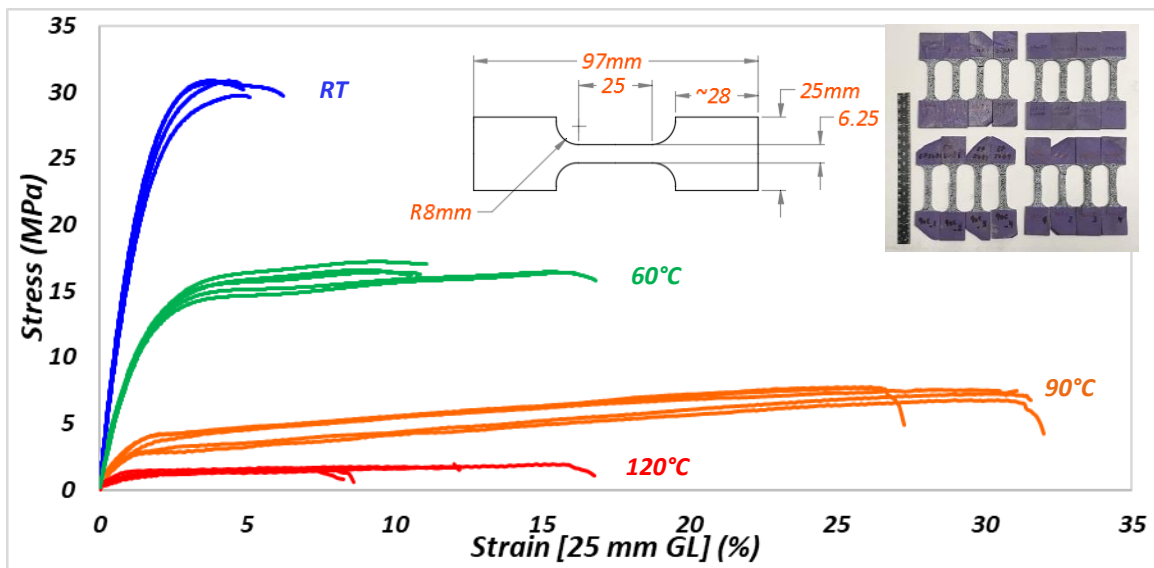


Figure 5. Stress-Strain curves for the adhesive EP5089 at different temperatures at strain rate 0.001/s

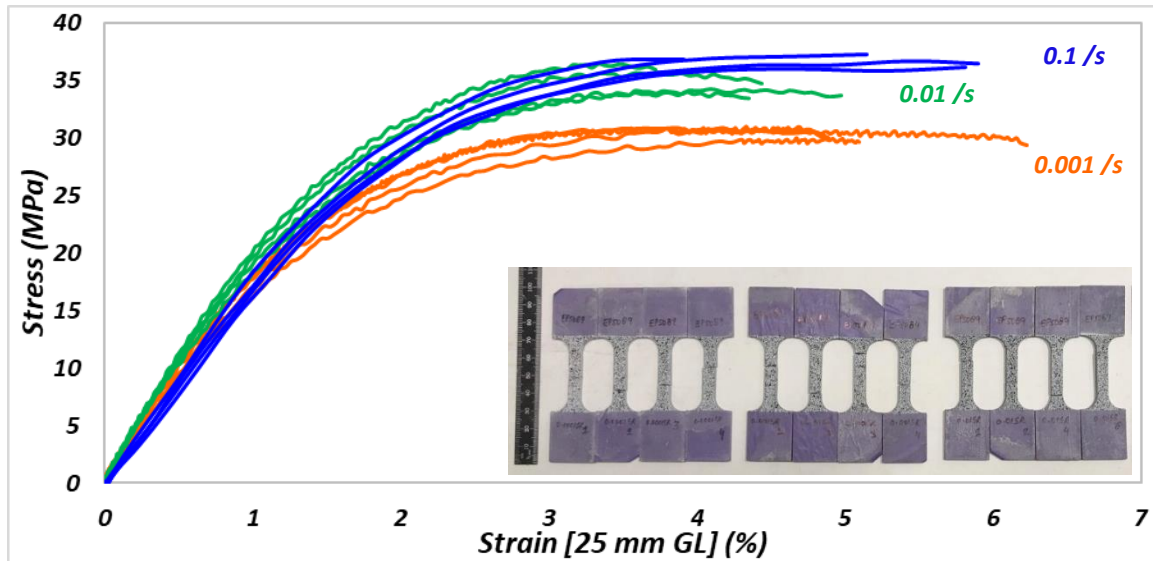


Figure 6. Stress-Strain curves for the adhesive EP5089 at different strain rates at room temperature

The stress-strain curves in Figure 5 show the temperature-dependent behavior of the strength and the modulus. With an increase in the temperature, there is a drop in the strength and the modulus of the adhesive. The tests at different strain rates (shown in Figure 6) show that the strength of the adhesive rises with the increase in the strain rate. The stress-strain curves of the adhesive can be closely compared to any metal, as they clearly show a linear slope in the beginning, followed by yielding and plastic behavior.

In the absence of any standard and for the sake of uniformity, the adhesive was assumed to yield at 2% strain and the flow curve beyond a strain of 2% was taken for plastic model fitting. The obtained plastic stress-strain curves were fit to the Johnson-Cook flow stress model and the best-fit parameters for the model are given in Table 3. The model best fit vs. experimental curves is shown in Figure 7 and Figure 8.

A' (MPa)	B (MPa)	C	m	n	T ₀ (K)	T _m (K)	$\dot{\epsilon}_{REF}(1/s)$
4.5	20.5	0.078	1.66	0.18	333	408	0.001

Table 3. J-C model parameters for EP5089 adhesive Eq. (8)

It is clear in Figure 7 that the trend in the hardening of the stress-strain curves lowers with increasing temperature, except the curve at 90°C which is an anomaly. Considering the general level of yield stresses, the J-C model captures the stress-strain curves at different temperatures and strain rates but is not able to capture the change in the hardening at 90°C.

Thus, the adhesive material models (i) curing kinetics model and (ii) viscoelastic mechanical model (iii) Plastic mechanical model were calibrated for EP5089. In the next section, an explicit formulation of the material models for a user-defined material subroutine in LS-DYNA is discussed.

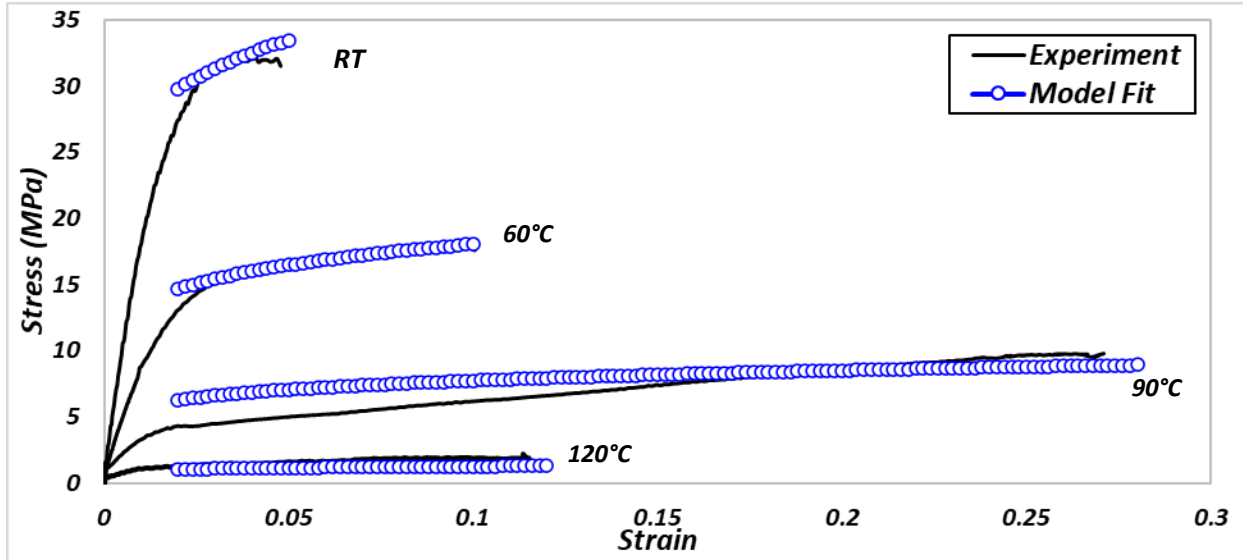


Figure 7. Experiment vs. J-C model fit for stress-strain curves at different temperatures

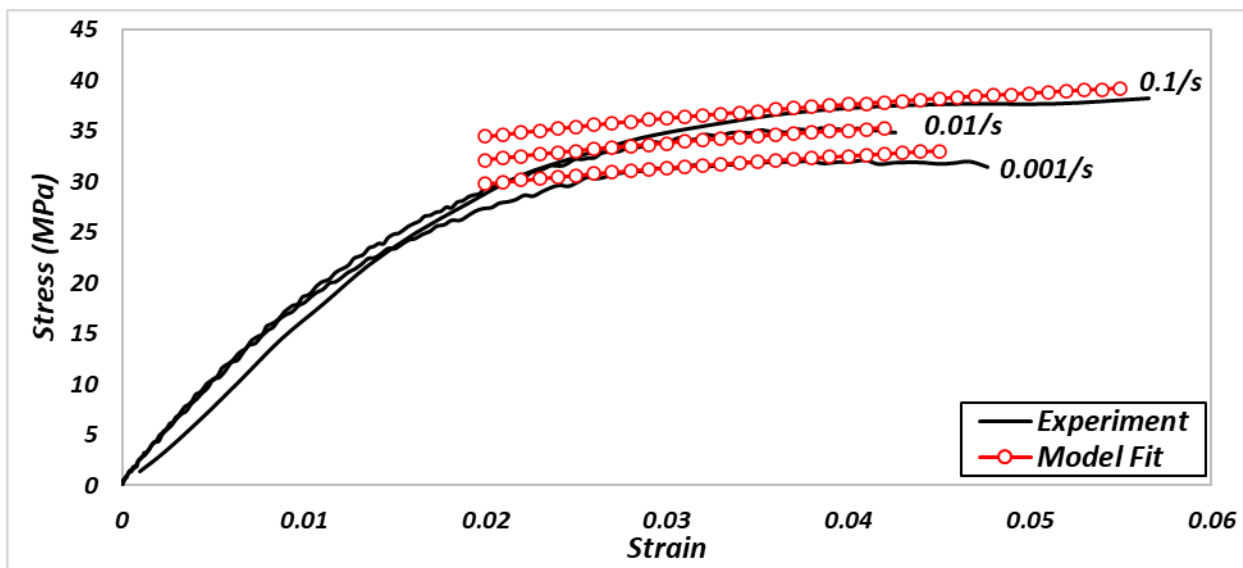


Figure 8. Experiment vs. J-C model fit for stress-strain curves at different strain rates

4. USER-DEFINED MATERIAL SUBROUTINE (UMAT) IMPLEMENTATION

The material subroutine formulation was based on the incremental theory of plasticity [31]. According to this theory, the strain increment for each time step 'n', the previous stress state 'n-1', and other history variables are provided to the code and are used in solving the stress state of the current time step 'n'. The code initially assumes that the strain increment in the time step is viscoelastic, and a viscoelastic predictor stress state called trial stress is calculated using the viscoelastic material model. The code then calculates the effective stress and compares it to the yield stress at that total strain which is calculated using the plastic flow stress constitutive model. If the effective stress at the time step exceeds the flow stress, it

represents that the material has yielded. The stresses are then cut back by the plastic corrector term to fall on the flow stress curve using the cutting plane algorithm. After several iterations, a converged value of plastic strain and stress state is obtained and is reported back to the program.

4.1. Implementation of viscoelastic material description

The implementation of the viscoelastic model was based on a generalized Maxwell element. Considering a purely isochoric viscoelastic behavior, the stress tensor for the next time step is the sum of the pure elastic stress and a factor governing the viscoelastic contribution from each branch of the generalized Maxwell element:

$$dev \underline{\sigma}^{n+1} = dev \underline{\sigma}_0^{n+1} + \sum_{j=1}^N \underline{h}_j^{n+1} \quad (11)$$

Where n is the time step and N is the number of branches in the Maxwell model. The elastic stress follows the basic linear-elastic relationship given in Eq. (12) with $\bar{\mathbb{C}}^e$ being the isotropic elasticity tensor.

$$\underline{\sigma}_0^{n+1} = \bar{\mathbb{C}}^e \underline{\varepsilon}^{n+1} \quad (12)$$

The vectors \underline{h}_j are internal state variables (isochoric part) for each branch j of the Maxwell element which account for the stress contribution due to the viscoelastic behavior. They describe the relaxation behavior in terms of the decay of stresses. Similarly, the vectors v_j are internal state variables for the volumetric part.

The isotropic elasticity tensor operator in Eq. (12) is:

$$\bar{\mathbb{C}}^e = \lambda \underline{\mathbf{1}} \otimes \underline{\mathbf{1}} + 2G_\infty \bar{\mathbb{I}} \quad (13)$$

If $\lambda = (K_\infty - 2/3G_\infty)$ and G_∞ are the first and second Lamé constants and $(\underline{\mathbf{1}} \otimes \underline{\mathbf{1}})_{ijkl} = \delta_{ij}\delta_{kl}$ and $\bar{\mathbb{I}}_{ijkl} = \frac{1}{2}(\delta_{ik}\delta_{jl} + \delta_{il}\delta_{jk})$ are the second-order and symmetric fourth-order identity tensors respectively.

Applying the same relationship for the viscoelastic decay of stresses also to the volumetric stress, the stress tensor for the step $n+1$ can be calculated from the given equation:

$$\underline{\sigma}^{n+1} = dev \underline{\sigma}^{n+1} + \frac{1}{3} tr \underline{\sigma}^{n+1} \underline{\mathbf{1}} = dev \underline{\sigma}_0^{n+1} + \sum_j \underline{h}_j^{n+1} + \left(K_\infty \varepsilon_V^{n+1} + \sum_j v_j^{n+1} \right) \underline{\mathbf{1}} \quad (14)$$

Because

$$tr \underline{\sigma}^{n+1} = 3 K_\infty \varepsilon_V^{n+1} \quad (15)$$

The evolution of the history variables \underline{h}_j^{n+1} and v_j^{n+1} is defined by the following expressions given in Eq. (16) and (17).

For the isochoric part,

$$\underline{h}_j^{n+1} = \exp\left(-\frac{\Delta t}{\beta_j}\right) \underline{h}_j^n + \gamma_j \frac{1 - \exp\left(-\frac{\Delta t}{\beta_j}\right)}{\frac{\Delta t}{\beta_j}} [dev \underline{\sigma}_0^{n+1} - dev \underline{\sigma}_0^n] \quad (16)$$

For the volumetric part,

$$v_j^{n+1} = \exp\left(-\frac{\Delta t}{\kappa_j}\right) v_j^n + k_j \frac{1 - \exp\left(-\frac{\Delta t}{\kappa_j}\right)}{\frac{\Delta t}{\kappa_j}} K_\infty \Delta \varepsilon_V \quad (17)$$

In these expressions, the relaxation functions are defined in a normalized form, i.e., instead of the shear modulus and the bulk modulus the dimensionless values $\gamma_j = \frac{G_j}{G_\infty}$ and $k_j = \frac{K_j}{K_\infty}$ are used.

$$dev \underline{\sigma}_0^n = \underline{\sigma}_0^n - \frac{1}{3} tr(\underline{\sigma}_0^n) \underline{1} = \bar{\bar{C}}^e \underline{\varepsilon}^n - K_\infty \varepsilon_V^n \underline{1} \quad (18)$$

The last term in Eq. (16) may now be transformed in the following way:

$$\begin{aligned} dev \underline{\sigma}_0^{n+1} - dev \underline{\sigma}_0^n &= dev (\underline{\sigma}_0^{n+1} - \underline{\sigma}_0^n) = dev(\bar{\bar{C}}^e \underline{\varepsilon}^{n+1} - \bar{\bar{C}}^e \underline{\varepsilon}^n) \\ &= dev(\bar{\bar{C}}^e \Delta \underline{\varepsilon}) = \bar{\bar{C}}^e \Delta \underline{\varepsilon} - K_\infty \Delta \varepsilon_V \underline{1} \end{aligned} \quad (19)$$

Substituting Eq. (19) into (16) gives

$$\underline{h}_j^{n+1} = \exp\left(-\frac{\Delta t}{\beta_j}\right) \underline{h}_j^n + \gamma_j \frac{1 - \exp\left(-\frac{\Delta t}{\beta_j}\right)}{\frac{\Delta t}{\beta_j}} [\bar{\bar{C}}^e \Delta \underline{\varepsilon} - K_\infty \Delta \varepsilon_V \underline{1}] \quad (20)$$

An equation for the stress update can be derived using Eq. (14)

$$\begin{aligned} \underline{\sigma}^{n+1} &= \frac{1}{3} tr \underline{\sigma}_0^{n+1} + \sum_j v_j^{n+1} \underline{1} + dev \underline{\sigma}_0^{n+1} + \sum_j \underline{h}_j^{n+1} \\ &= \underline{\sigma}_0^{n+1} + \sum_j v_j^{n+1} + \sum_j \underline{h}_j^{n+1} \\ &= \bar{\bar{C}}^e \underline{\varepsilon}^{n+1} + \sum_j v_j^{n+1} \underline{1} + \sum_j \underline{h}_j^{n+1} \end{aligned} \quad (21)$$

The above equations were changed to Voigt notation to develop a FORTRAN algorithm that can be used to implement in a user-defined material subroutine in LS-DYNA.

$$\begin{aligned} \underline{\sigma} &= (\sigma_{11} \ \sigma_{22} \ \sigma_{33} \ \sigma_{12} \ \sigma_{23} \ \sigma_{13})^t \\ \underline{\varepsilon} &= (\varepsilon_{11} \ \varepsilon_{22} \ \varepsilon_{33} \ \varepsilon_{12} \ \varepsilon_{23} \ \varepsilon_{13})^t \end{aligned} \quad (22)$$

In this notation, the first term of Eq. (21) has the following form:

$$\begin{aligned}
\bar{\underline{C}}^e \underline{\varepsilon}^{n+1} &= \begin{bmatrix} \lambda + 2G_\infty & \lambda & \lambda & 0 & 0 & 0 \\ \lambda & \lambda + 2G_\infty & \lambda & 0 & 0 & 0 \\ \lambda & \lambda & \lambda + 2G_\infty & 0 & 0 & 0 \\ 0 & 0 & 0 & 2G_\infty & 0 & 0 \\ 0 & 0 & 0 & 0 & 2G_\infty & 0 \\ 0 & 0 & 0 & 0 & 0 & 2G_\infty \end{bmatrix} \underline{\varepsilon}^{n+1} \\
&= \begin{bmatrix} 2G_\infty \varepsilon_{11}^{n+1} + \lambda(\varepsilon_{11}^{n+1} + \varepsilon_{22}^{n+1} + \varepsilon_{33}^{n+1}) \\ 2G_\infty \varepsilon_{22}^{n+1} + \lambda(\varepsilon_{11}^{n+1} + \varepsilon_{22}^{n+1} + \varepsilon_{33}^{n+1}) \\ 2G_\infty \varepsilon_{33}^{n+1} + \lambda(\varepsilon_{11}^{n+1} + \varepsilon_{22}^{n+1} + \varepsilon_{33}^{n+1}) \\ 2G_\infty \varepsilon_{12}^{n+1} \\ 2G_\infty \varepsilon_{23}^{n+1} \\ 2G_\infty \varepsilon_{13}^{n+1} \end{bmatrix} \quad (23) \\
&= \begin{bmatrix} 2G_\infty \varepsilon_{11}^{n+1} + \lambda \varepsilon_V^{n+1} \\ 2G_\infty \varepsilon_{22}^{n+1} + \lambda \varepsilon_V^{n+1} \\ 2G_\infty \varepsilon_{33}^{n+1} + \lambda \varepsilon_V^{n+1} \\ 2G_\infty \varepsilon_{12}^{n+1} \\ 2G_\infty \varepsilon_{23}^{n+1} \\ 2G_\infty \varepsilon_{13}^{n+1} \end{bmatrix}
\end{aligned}$$

The last term in Eq. (21) looks like this in the Voigt notation:

$$\bar{\underline{C}}^e \Delta \underline{\varepsilon} - K_\infty \Delta \varepsilon_V \underline{1} = \begin{bmatrix} 2G_\infty \Delta \varepsilon_{11} + \lambda \Delta \varepsilon_V \\ 2G_\infty \Delta \varepsilon_{22} + \lambda \Delta \varepsilon_V \\ 2G_\infty \Delta \varepsilon_{33} + \lambda \Delta \varepsilon_V \\ 2G_\infty \Delta \varepsilon_{12} \\ 2G_\infty \Delta \varepsilon_{23} \\ 2G_\infty \Delta \varepsilon_{13} \end{bmatrix} - K_\infty \begin{bmatrix} \Delta \varepsilon_V \\ \Delta \varepsilon_V \\ \Delta \varepsilon_V \\ 0 \\ 0 \\ 0 \end{bmatrix} \quad (24)$$

Substituting Eq. (24) into (20) gives

$$\underline{h}_j^{n+1} = \exp\left(-\frac{\Delta t}{\beta_j}\right) \begin{bmatrix} h_{j,11}^n \\ h_{j,22}^n \\ h_{j,33}^n \\ h_{j,12}^n \\ h_{j,23}^n \\ h_{j,13}^n \end{bmatrix} + \gamma_j \frac{1 - \exp\left(-\frac{\Delta t}{\beta_j}\right)}{\frac{\Delta t}{\beta_j}} \begin{bmatrix} 2G_\infty \Delta \varepsilon_{11} + (\lambda - K_\infty) \Delta \varepsilon_V \\ 2G_\infty \Delta \varepsilon_{22} + (\lambda - K_\infty) \Delta \varepsilon_V \\ 2G_\infty \Delta \varepsilon_{33} + (\lambda - K_\infty) \Delta \varepsilon_V \\ 2G_\infty \Delta \varepsilon_{12} \\ 2G_\infty \Delta \varepsilon_{23} \\ 2G_\infty \Delta \varepsilon_{13} \end{bmatrix} \quad (25)$$

The above equations were transferred to a FORTRAN subroutine. The parameters required for the viscoelastic material law coded in the material subroutine are G_0 instantaneous shear modulus; G_j, β_j shear modulus and shear relaxation time for the j^{th} branch of the generalized Maxwell element; K_0 instantaneous bulk modulus; K_j, κ_j bulk modulus and bulk relaxation time of the j^{th} branch of the generalized Maxwell element.

4.2. Implementation of plastic constitutive equation

In terms of incremental stress updates used by typical FEA codes, the viscoelastic stress result is the predictor stress or trial stress and now the plastic corrector step needs to be added if the yield limit is exceeded.

The formulation was based on the isotropic Von-Mises yield function to calculate the effective stress from the stress state.

$$\bar{\sigma} = \sqrt{\frac{1}{2}[(\sigma_{11} - \sigma_{22})^2 + (\sigma_{22} - \sigma_{33})^2 + (\sigma_{33} - \sigma_{11})^2 + 6(\sigma_{12}^2 + \sigma_{23}^2 + \sigma_{13}^2)]} \quad (26)$$

The flow stress used in the formulation was based on the Johnson-Cook flow stress model, given in Eq. (8), (9), and (10).

The yield function represented by Eq. (26) can be written as:

$$\phi(\bar{\sigma}, \bar{\varepsilon}^P, \dot{\varepsilon}, T) = \bar{\sigma}(\underline{\sigma}, T) - H(\bar{\varepsilon}^P, \dot{\varepsilon}, T) = 0 \quad (27)$$

where H is the hardening rule defined by Eq. (8). T is the temperature during the thermal time step.

The equations used for iteratively integrating the plastic constitutive equations for rate and temperature-dependent plasticity with associated flow rule are:

$$\text{Associative flow rule: } \dot{\varepsilon}^P = \dot{\lambda} \frac{d\phi}{d\underline{\sigma}} \quad (28)$$

$$\text{Yield Function: } \phi \leq 0 \quad (29)$$

$$\text{Normality parameter: } \dot{\lambda} \geq 0 \quad (30)$$

$$\text{Kuhn-Tucker condition: } \dot{\lambda} \phi = 0 \quad (31)$$

$$\text{Consistency condition: } \dot{\lambda} \dot{\phi} = 0 \quad (32)$$

where $\dot{\lambda}$ is the plastic multiplier.

4.4. Verification of the Modeling Approach:

4.4.1. Verification of Curing Kinetics and Viscoelastic model

The material subroutine was tested and debugged on simple single-element finite element models. This approach was used to eliminate the effects of other parameters and isolate the performance of the individual components. An uncured element was modeled to cure on a temperature cycle of 100°C to 250°C at different heating rates and the cure vs. time model prediction was compared to the mathematical results.

The viscoelastic model was also verified using a single element model for a variety of scenarios. The material subroutine was used with the plastic model turned off to isolate the viscoelastic behavior. For a strain of 10%, the stress response was extracted as an output from the LS-DYNA model. The stress vs. time and imposed strain were used to calculate the modulus vs. time. The model was tested for different temperatures and the modulus relaxation curves obtained from the FE model at different temperatures were compared to the shifted master curves at the modeled temperatures.

4.4.2. Verification of viscoelastic-plastic coupled model

The verification of the coupled response of the viscoelastic-plastic model was performed on a finite element simulation on the tensile specimen geometry. The material subroutine was used with the plastic model turned on, to get a combined response of viscoelastic and plastic models. The simulations were run for a fully cured adhesive at 20°C, 60°C, 90°C, 120°C at a constant strain rate of 0.001/s. The predictions from the finite element model were in excellent agreement with the experimental stress-strain curves, as shown in Figure 9. The slopes of the curve in the beginning determined by the viscoelastic model matches the experimentally obtained stress-strain curves. Although the viscoelastic model was calibrated using DMA data acquired in shear deformation mode, the predicted modulus values in tensile mode agree with the young's modulus values obtained from the tensile tests. There are no significant negative effects of the modeling assumptions as the yield values and the trend of the plastic curves at different temperatures matched with the experimental tensile curves. This was an assurance that the modeling approach was reliable and could be trusted for complex simulations.

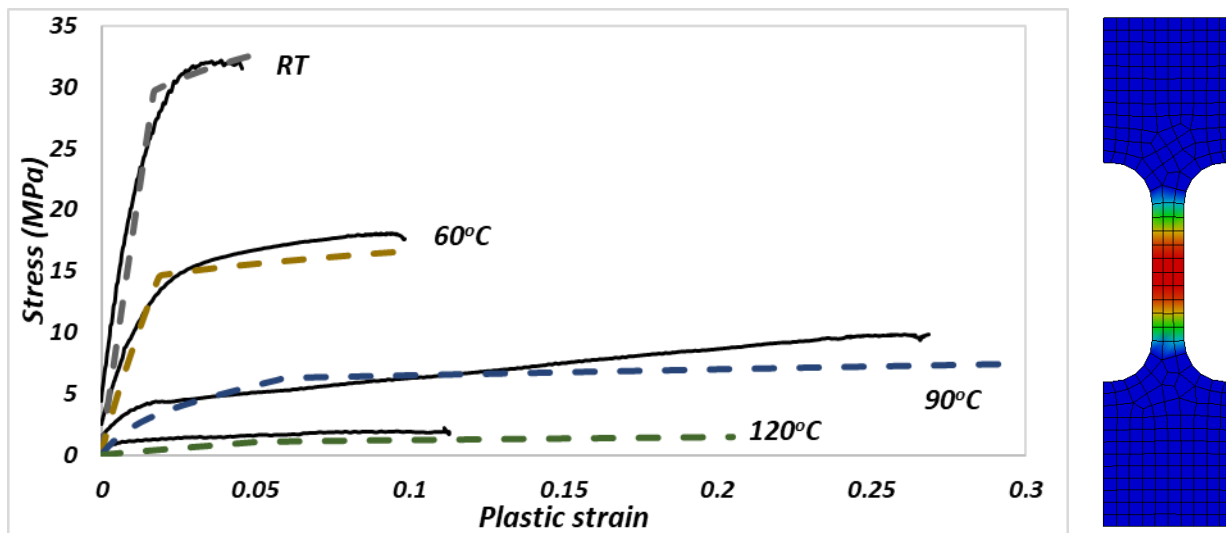


Figure 9. (a) Viscoelastic-plastic model performance in FE simulation (dashed lines) vs. experimental stress-strain curves (solid lines); (b) Geometry used for FE simulation

5. COMPONENT LEVEL VALIDATION – SCALED-DOWN ROOF MODEL

5.1. Experiments on scaled-down roof model

The modeling approach and the user-defined material subroutine were validated at the component level by curing an adhesive bonded automotive roof panel in a controlled environment and studying the thermal effects on the structure.

5.1.1. Experimental setup

The experimental setup (shown in *Figure 10*) used for the component level validation consisted of a heating chamber with a wide glass window opening on one door, to enable optical strain measurements using DIC. Four thermocouples were attached to the specimen to record the temperature profile on the surface of the specimen. During the curing process, the displacements in the roof panel and the roof bows due to the thermal expansion and contraction were recorded by GOM ARAMIS 5-Megapixel 3D-DIC to capture the distortion in the structure during the heating and cooling phase of the automotive paint baking cycle. The use of 3D-DIC enabled full-field displacements on the specimen surface in the 3D space. The temperature signal was fed to the DIC system to synchronize the time-temperature-displacement signals.

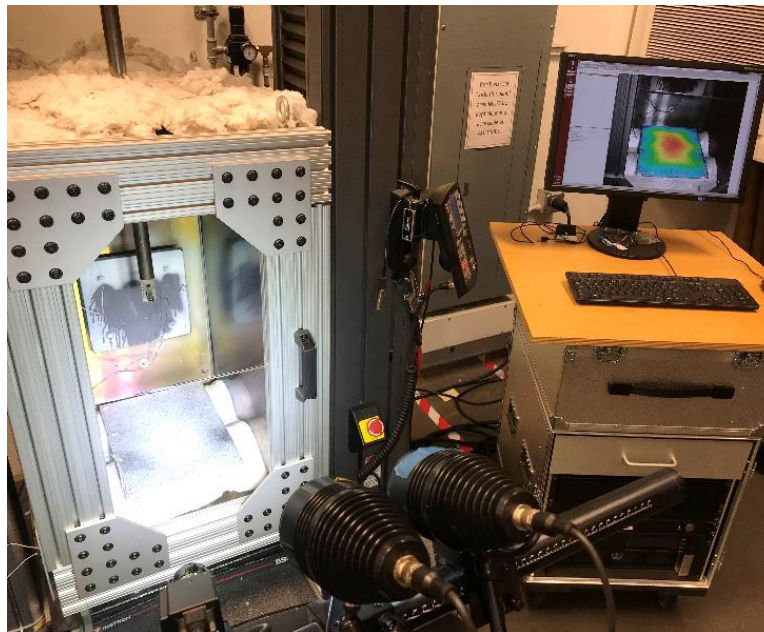


Figure 10. Experimental setup for component-level validation on a scaled-down roof model

5.1.2. Specimen Details

The scaled-down roof component was a 1/6th scaled-down model of SUV roof (1900 mm x 1100 mm). The roof component consisted of steel roof rails made of U-channel (3 mm thick) welded together to form a rigid frame. The steel frame was 320 mm x 220 mm in size which had a flat aluminum panel (1.1 mm thick AA5754-O sheet) of 300 mm x 200 mm bonded to it. An adhesive layer of 0.2 mm with a bondline width of 10 mm was applied to the steel frame. *Figure 11* shows the welded steel frame, adhesive applied on the target area and aluminum flat panel positioned on top of the steel frame and adhesive.

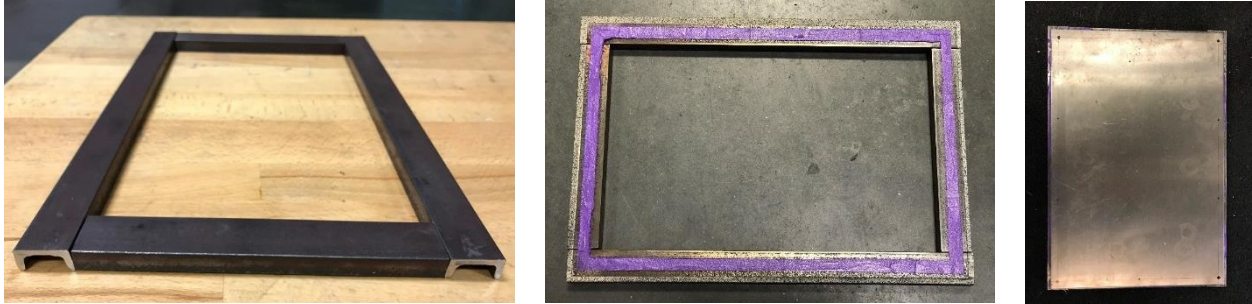


Figure 11. (a) Steel frame; (b) adhesive applied on the frame; (c) aluminum flat panel mounted on the frame

The tests were conducted in two scenarios:

- *Scenario 1*: Roof panel joined to the bows with adhesive only
- *Scenario 2*: Roof panel joined to the bows with adhesive and mechanical fixations

Scenario 1 (with adhesive only): In this case, the top left corner of the component was clamped with a heavy-duty C-Clamp to lock the movement in X, Y, and Z directions. The other three corners were held together by spring clamps to lock only the movement in Z-direction and to ensure proper bonding to the adhesive. The specimen for scenario 1 is shown in *Figure 13(a)*.

Scenario 2 (with adhesive and mechanical fixation): In this case, the flat aluminum panel was stuck on the steel frame with adhesive and held together by Friction Element Welds (FEW) by EJOT Corporation at a gap of 100 mm. FEW is an innovative option to join different materials and semi-finished multi-material parts, especially lightweight materials such as aluminum and advanced high-strength steel. A requirement for this method is the accessibility of the joining point on both sides. This was one of the reasons for choosing a steel U-slot for building the frame of the roof component. For the scope of this study, FEWs can simply be considered as rigid mechanical fixations which ensure that the panel was locked in X, Y, and Z directions, and the expansion was limited at the weld locations. This scenario was closer to an actual roof construction in an automotive BIW. The specimen for scenario 2 with adhesive and mechanical fixation is shown in *Figure 14(a)*.

5.1.3. Test Process

After the specimens were prepared, the test specimen with uncured adhesive between the aluminum flat panel and steel frame was painted in speckle pattern, required for the DIC system. Two thermocouples were attached to the back of the aluminum panel and two were attached to the steel frame at locations shown in *Figure 12(a)*. The chamber was heated to 180°C for 45 minutes and then was let to cool down naturally. A sample temperature profile recorded during the test for the four thermocouples is shown in *Figure 12(b)*. The temperature at the rear rail, captured by thermocouple 1 was higher than the rest of the locations because of its proximity to the fan and heating elements of the heating chamber. The temperature profiles recorded from the experiments were later fed into the FE simulations. The test was stopped when the temperature dropped below 30°C.

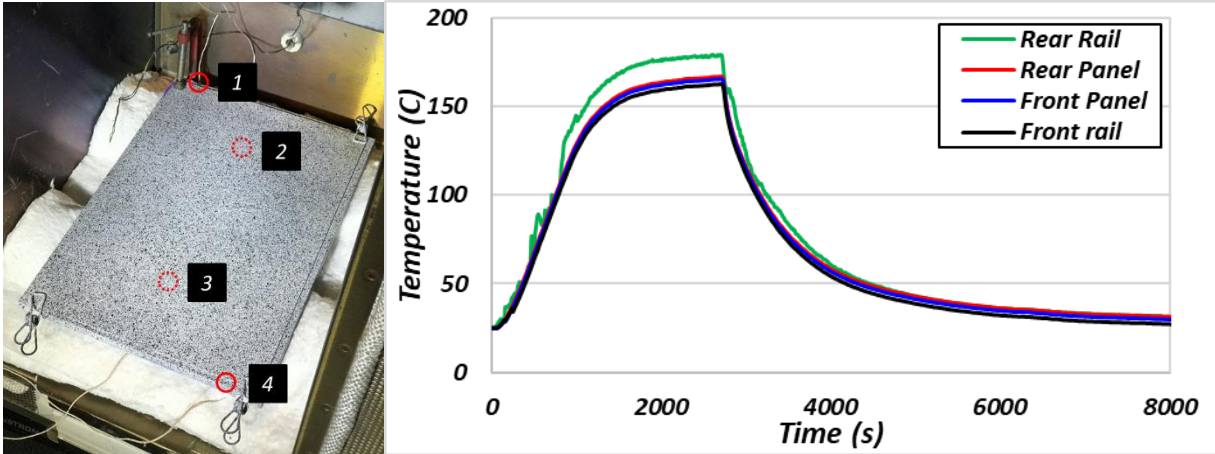


Figure 12. (a) Thermocouple locations; (b) Temperature profile for the curing cycle recorded by four thermocouples

5.2. Finite Element modeling

5.2.1. Model Geometry:

Model I (with adhesive only): The dimensions of the finite element model were identical to the test specimen. The steel frame was modeled by a single layer of solid elements of size 5mm. The aluminum flat panel was modeled using shell elements of size 5 mm. The property input for the steel and aluminum flat panel is given in Table 4. The adhesive was modeled by solid elements of size 2 mm and a bond thickness of 0.20 mm. The hard clamp in the top left of the test specimen was modeled using a single solid element. The finite element model geometry is shown in Figure 13(b).

The top and bottom surfaces of the adhesive elements were tied to the interacting surfaces of the aluminum panel and steel frame using *CONTACT_TIED_SURFACE_TO_SURFACE definition in LS-DYNA. The top and bottom surfaces of the solid element were tied to the aluminum panel and steel frame, like the adhesive. The steel frame and the aluminum panel were modeled using the material model *MAT_ELASTIC_PLASTIC_THERMAL which takes temperature-dependent properties of the material including coefficient of thermal expansion. The thermal material card used for the substrates, grips, and adhesive was *MAT_THERMAL_ISOTROPIC_TD_LC which takes the values for conductivity and specific heat capacity as a function of temperature.

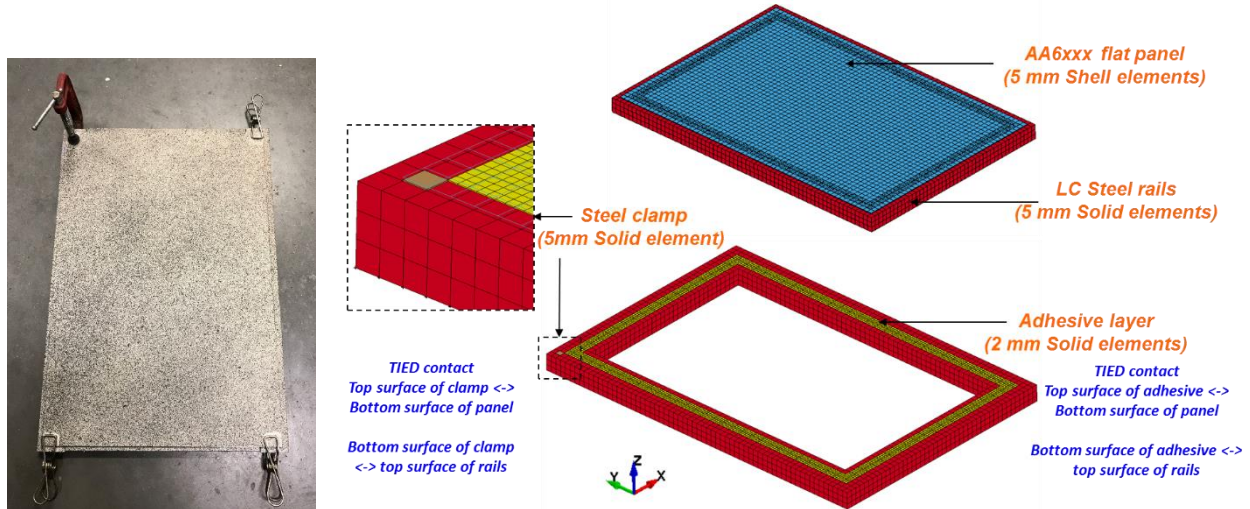


Figure 13. (a) Test Specimen with adhesive only; (b) Finite element model with adhesive only, clamped on the top left corner

Model II (with adhesive and mechanical fixation): The dimensions of the model were identical to the test specimen with adhesive and mechanical fixations. For this case, the steel frame was modeled by solid elements of size 1 mm, and the thickness of the steel frame was 5 mm. The aluminum flat panel was modeled using shell elements of size 8 mm, refined to 1 mm in the critical contact region. The adhesive was modeled using solid elements of size 2 mm and a bond thickness of 0.20 mm. The top and bottom surfaces of the adhesive elements were tied to the interacting surfaces of the aluminum panel and steel frame using *CONTACT_TIED_SURFACE_TO_SURFACE contact definition in LS-DYNA. The weld elements were modeled as octagonal solid geometries to replicate a circular weld of diameter 4 mm. The height of the weld element between the steel frame and aluminum panel was 0.2 mm. The weld element top and bottom surfaces were tied to the top panel and bottom frame by TIED contact, like the adhesive elements. The weld elements were spaced at a gap of 100 mm from each other identical to the actual test specimen, as shown in Figure 14(b). The property input for the steel, friction element weld and aluminum flat panel is given in Table 4.

Property	Steel Frame; Friction Element Weld (@298K - @573K)	AA5754 Flat Panel (@298K - @573K)
Young's Modulus	205 GPa – 200 GPa	69 GPa – 55 GPa
Yield Strength	650 MPa – 500 MPa	145 MPa – 80 MPa
CTE	1.10E-5 (1/K)	2.10E-5 (1/K)
Tangent Modulus	10 GPa – 6 GPa	10 GPa – 3 GPa

Thermal Conductivity	55 W/m K	230 W/m K
Density	7.87 g/cm ³	2.7 g/cm ³
Poisson's Ratio	0.28	0.33

Table 4. Material properties for steel rails, friction element welds and aluminum flat panel used in the FE model

5.3. Comparison of FE predictions with experimental results

The displacements in the aluminum panel captured during the test were compared to the displacements predicted by the finite element model. The comparison was made based on the general trend of displacement contour in the panel and point displacements at the top left, top right, bottom left, bottom right, and center point selected on the same location on the test specimen and the finite element model. The chosen point locations are shown in *Figure 15*.

5.3.1. Model I (with adhesive only)

The finite element predictions and DIC generated displacements from the experiments are shown in *Figures 16, 17, and 18*. The displacements in the X, Y, and Z directions are shown at the end of the heating phase and the cooling phase. As the temperature rises, the aluminum panel and the steel frame start expanding in the X and the Y direction. Since the adhesive is uncured at the beginning of the test, the adhesive does not pose any restriction to the expansion across the adhesive bond. As a result, the aluminum panel expands freely in the X and Y direction. At the peak temperature, near the end of the heating phase, the adhesive gets fully cured and starts restricting any further movement across the joint. In the cooling phase, as the whole structure starts to cool down, the aluminum panel and the steel frame start contracting to go back to their initial state. But the fully cured adhesive puts restrictions on the contraction of the panel with respect to the frame. As a result, the panel and the steel frame go into an unintended distorted state. There is a residual displacement in the X and Y direction in the panel.

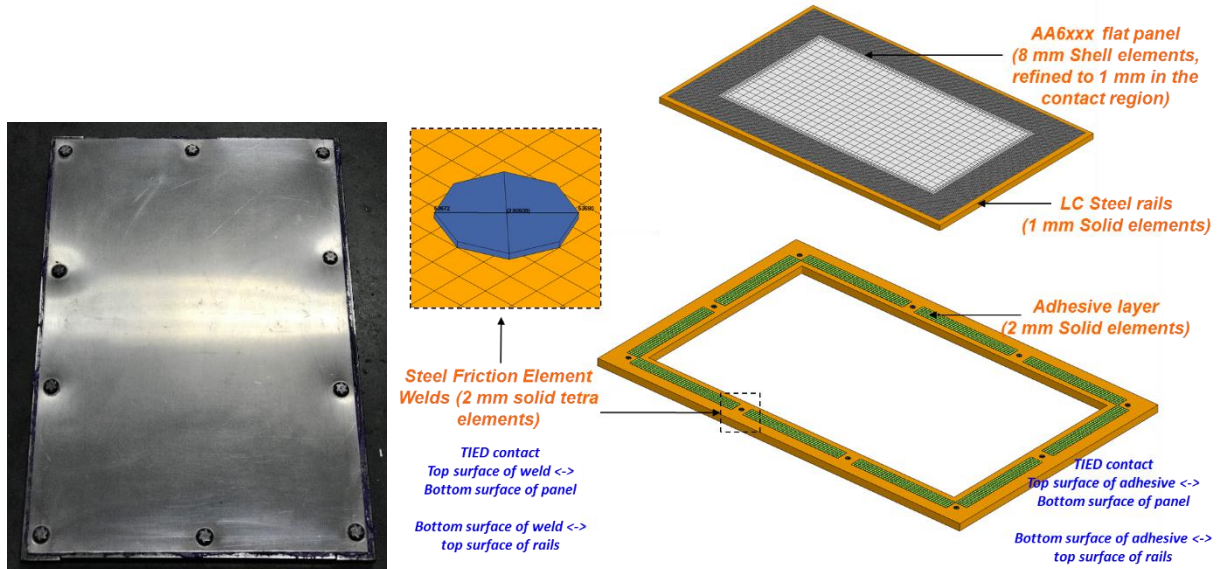


Figure 14. (a) Test specimen with adhesive and mechanical fixations; (b) Finite element model with adhesive and mechanical fixations

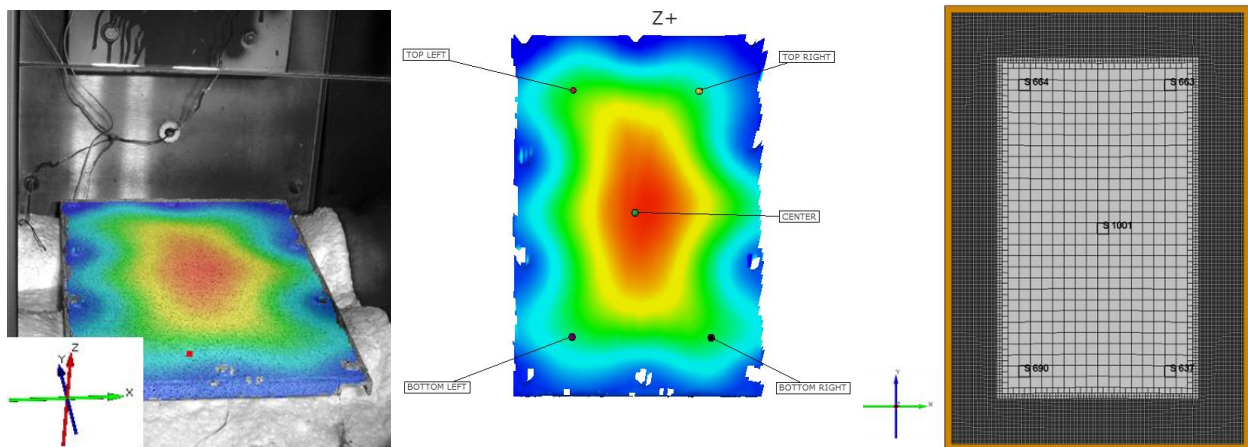


Figure 15. Points selected for comparison between the test and FE predictions in (a) DIC Strain Map; (b) FE model

This behavior is represented in the experiments as well as FE predictions. Having a hard constraint in the top left corner due to the clamp, the aluminum panel tends to expand more in the positive X direction and negative Y direction during the heating phase. At the end of the cooling phase, the magnitude of the displacements drops as a result of contraction, but there is a residual displacement due to the effect of the adhesive bond. The trend in the displacements in the X and Y direction are similar for the experiments and finite element predictions. Comparing the point displacements revealed that the values of Y-displacement in the experiments were shifted. A small global movement in the whole test specimen inside the furnace may cause the displacements to drift in a certain direction. To remove this global movement, the displacements in Y-direction were shifted by 0.3 mm in the positive direction. The magnitude of relative point displacements after adjusting the DIC values matched the FE predictions.

An important thing to note here is that the experiments were run inside a convection furnace with DIC cameras looking through a glass window at a slanting angle. It was a challenge to get meaningful

measurements in this scenario considering the difficulties in measurement due to heatwaves inside the furnace and distortion due to glass between the test specimen and the cameras. Considering the discussed challenges, the trend in the displacements in the experiments and finite element predictions agree with each other.

The displacements in the Z-direction in this case are not much dependent on the adhesive behavior. The experiments show that the panel had a variation in the Z-contour, which is not predicted by the finite element model. This behavior can be explained by looking into the initial state of the aluminum panel. The aluminum panel was modeled as a perfectly flat sheet in finite element, which is not the case in the experiment. When a metal sheet is heated to a certain temperature, the internal stresses due to rolling are released and the minor distortions in the panel are observed. This phenomenon could not be captured in the finite element simulations.

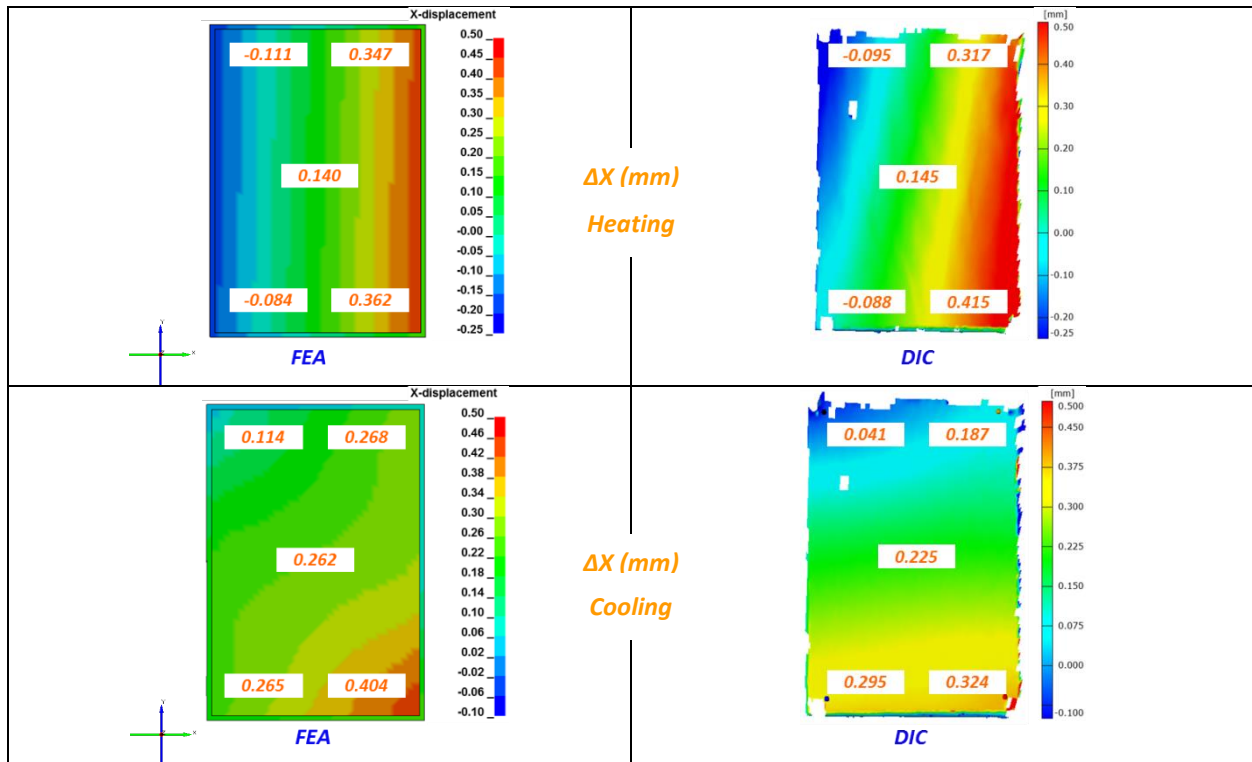


Figure 16. X-displacement (mm) prediction from finite element model vs. DIC generated values for Model-I (with adhesive only) at the end of heating phase and cooling phase

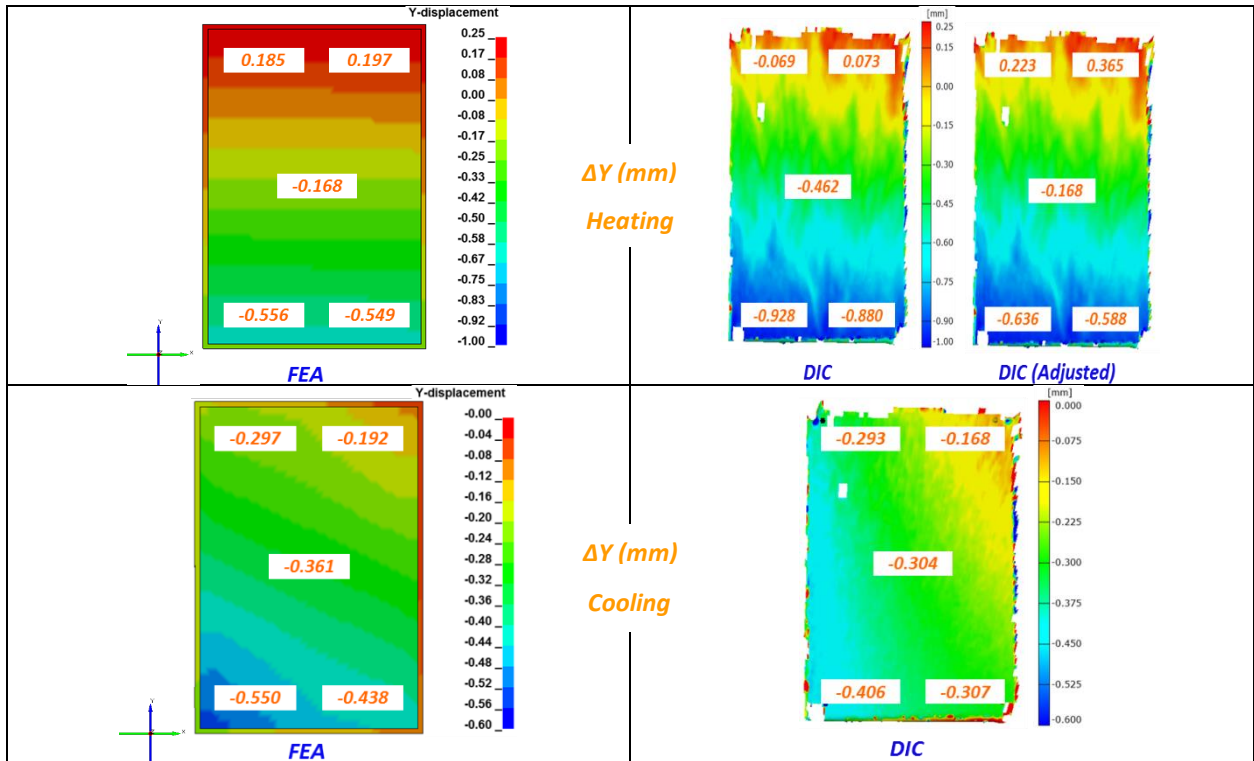


Figure 17. Y-displacement (mm) prediction from finite element model vs. DIC generated values for Model-I (with adhesive only) at the end of heating phase and cooling phase

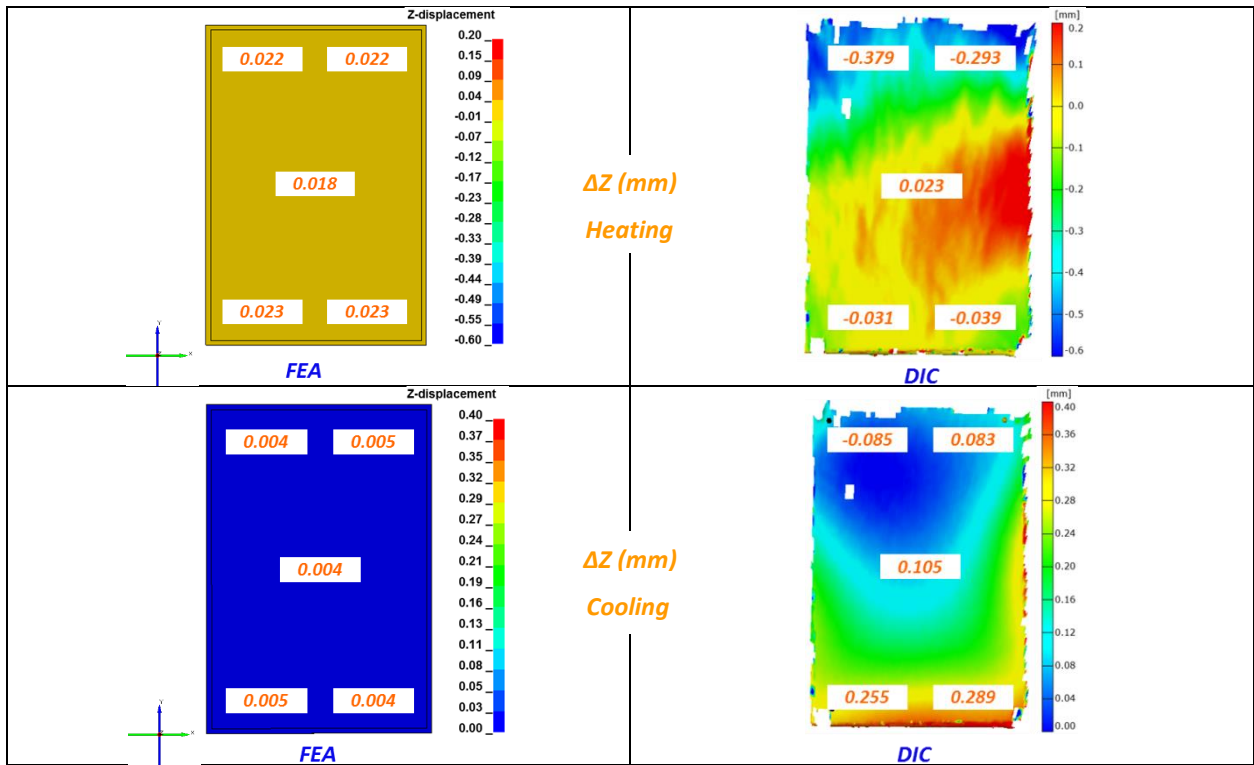


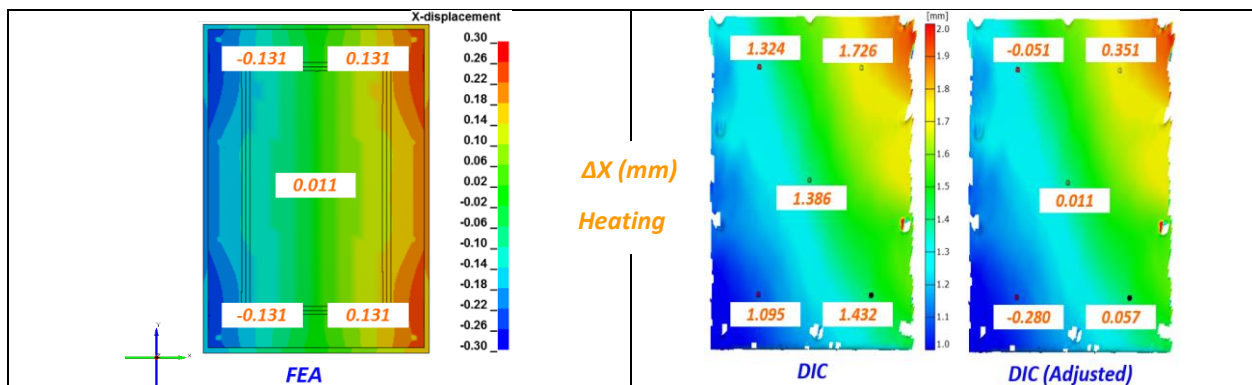
Figure 18. Z-displacement (mm) prediction from finite element model vs. DIC generated values for Model-I (with adhesive only) at the end of heating phase and cooling phase

5.3.2. Model II (with adhesive and mechanical fixations)

The finite element predictions and DIC generated displacements from the experiments with adhesive and mechanical fixations are shown in Figures 19, 20, and 21. The displacements in the X, Y, and Z directions are shown at the end of the heating phase and the cooling phase. In this case, the aluminum panel was locked in four directions due to the friction element welds in the periphery of the panel. As the temperature rises, the aluminum panel and the steel frame start expanding in the X and the Y direction but are constrained in those directions due to the friction element welds. As a result, the aluminum panel starts to bulge up in the Z-direction. Since the adhesive is uncured at the beginning of the test, the adhesive does not play a major role in the behavior of the roof component in the heating phase. As a result, the aluminum panel expands in the Z-direction. Due to the mechanical fixations, the X and Y displacements across the adhesive bond are much smaller in magnitude as compared to model I.

This behavior is represented in the experiments as well as FE predictions. The presence of friction element welds in the circumference of the panel locks the movement in the X and Y directions. Therefore, at the end of the heating phase, the X and Y-displacements in the panel are negligible as compared to the model I, while the bulging in the Z-direction is significant. At the end of the cooling phase, the magnitude of the displacements drops but leaves a residual displacement because of the fully cured adhesive bond. The trend in the displacements in the X, Y, and Z directions are similar for the experiments and finite element predictions. The global movement in the panel was compensated by shifting the displacements in the X and Y-direction to match the displacement of the center point.

Since this case and type of construction is closer to an actual scenario where the roof panel is adhesively bonded to the steel roof bows and fixed by mechanical fixations, the displacements in the Z-direction are of significance. This bulge in the center of the aluminum panel due to the constraints in the circumference causes severe distortion in the roof component. The aluminum panel was modeled as a perfectly flat sheet in finite element, which although is not the case in the experiment, but the magnitude of upward bulging in the panel is high enough to compensate for minor variations in the initial flatness of the panel.



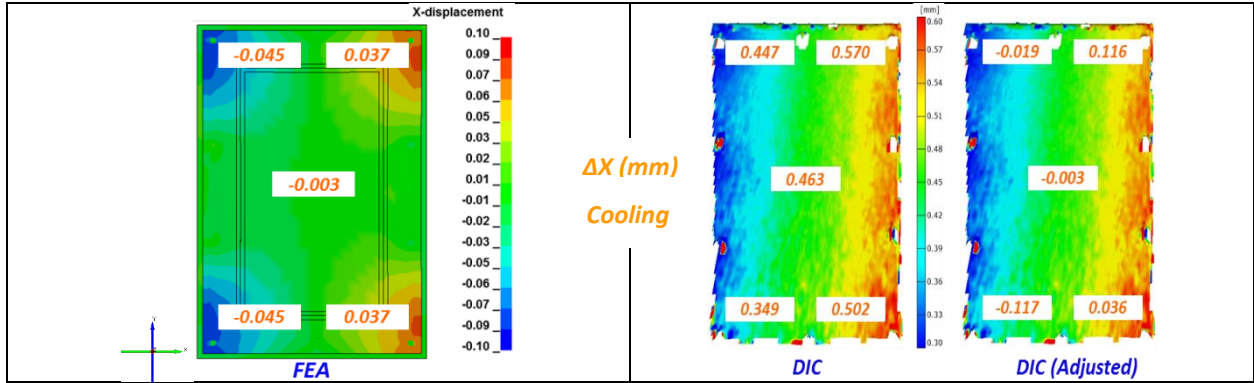


Figure 19. X-displacement (mm) prediction from finite element model vs. DIC generated values for Model II (with adhesive and mechanical fixations) at the end of heating phase and cooling phase

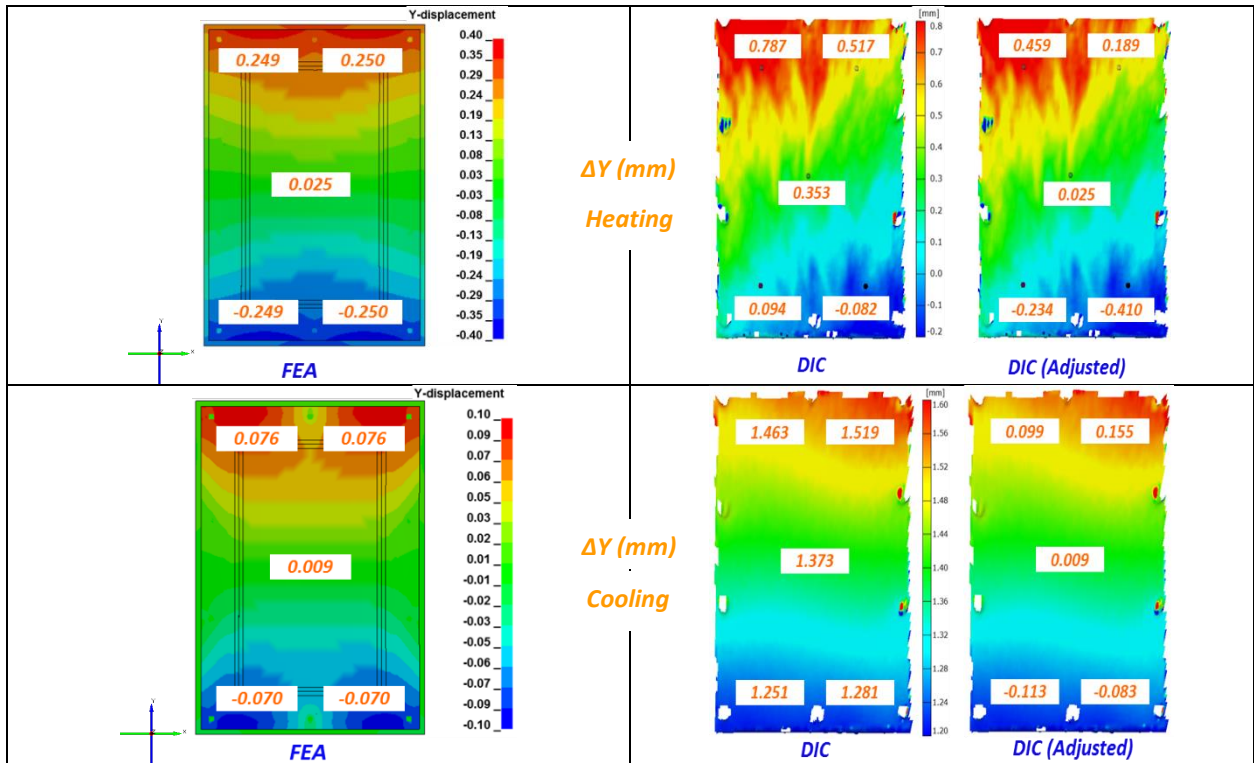


Figure 20. Y-displacement (mm) prediction from finite element model vs. DIC generated values for Model II (with adhesive and mechanical fixations) at the end of heating phase and cooling phase

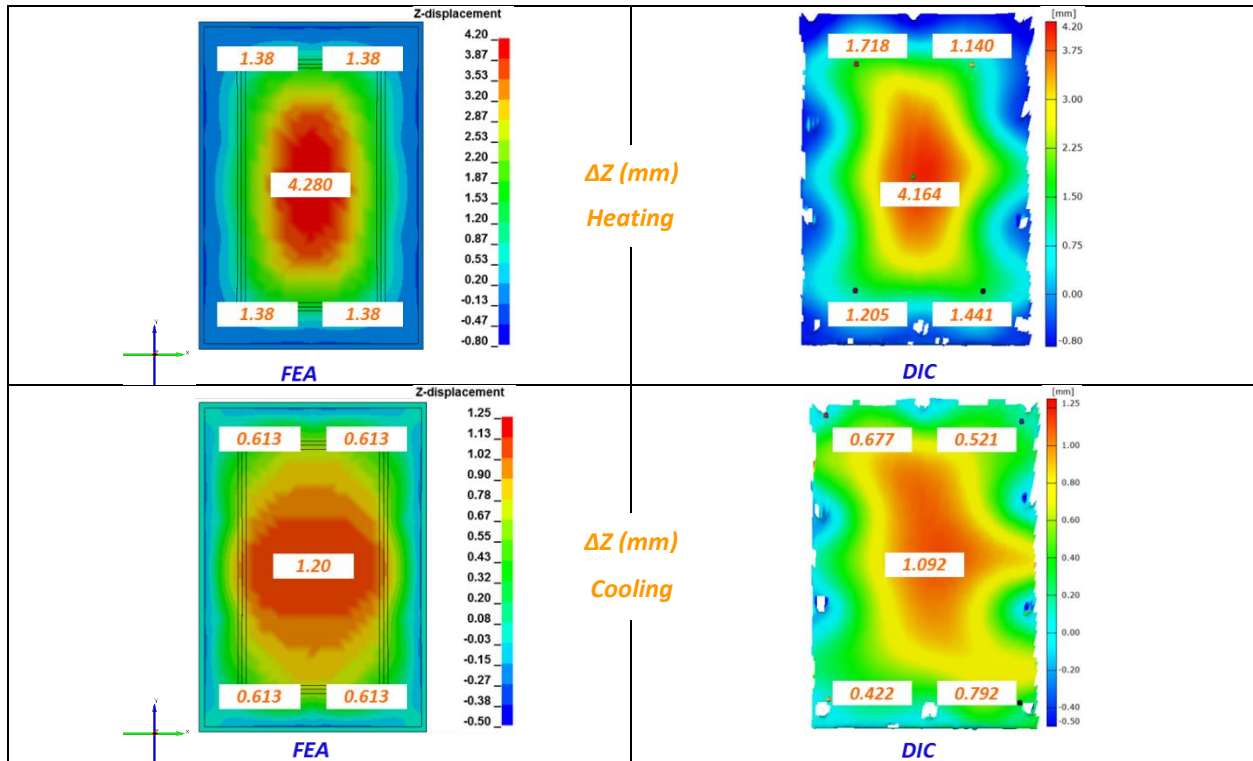


Figure 21. Z-displacement (mm) prediction from finite element model vs. DIC generated values for Model II (with adhesive and mechanical fixations) at the end of heating phase and cooling phase

5.4. Computational Results

The finite element model was validated with the experimental results by comparing the general trend of the X, Y, and Z displacements and the relative point displacements of chosen five points on the surface of the aluminum panel. Since the FE model predictions were in agreement with the experiments, the predictions of residual stress state and magnitude in the adhesive bond can be studied with confidence. The residual stresses developed in the adhesive joint in models I and II are shown in *Figure 22*. If the magnitude of stresses in the adhesive bond is compared to the plastic stress-strain curve of the fully cured adhesive, it accounts for approximately 25% of the yield limit of the adhesive. Such a high level of stress in the adhesive bond is detrimental to the performance of the adhesive bond in the life cycle of the roof component.

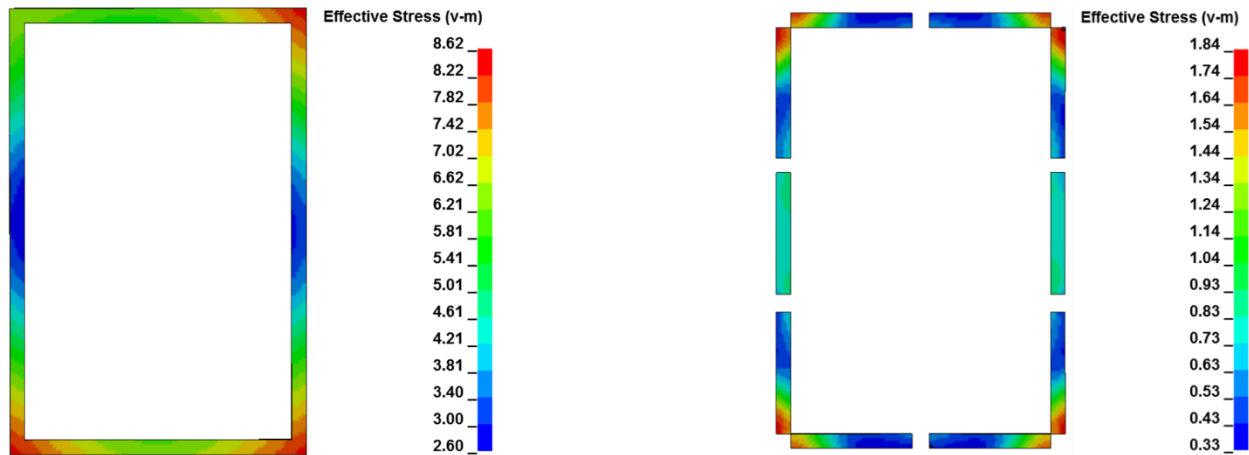


Figure 22. Effective residual stress (MPa) in the adhesive bond for (a) model I: with adhesive only; (b) model II: with adhesive and mechanical fixations

Effect of mechanical fixations: The finite element predictions of the effective stress in the adhesive bond for model I and model II show that the addition of mechanical fixations to the model lowers the magnitude of the effective residual stresses. This is due to constraints in the X, Y directions which allow a lower level of displacement across the adhesive bondline. The presence of mechanical fixations drops the residual stresses to ~5% of the yield limit of the adhesive. Therefore, the presence of mechanical fixations is better for the adhesive bond.

Although the presence of fixations in the structure is good for the adhesive bond, it proves to be bad for the geometrical accuracy of the structure. It was observed that the upward bulge in the Z-direction was over 4mm for a 1/6th scaled-down model with a relatively high thickness to width ratio of the aluminum panel.

The magnitude of upward bulging in the roof panel was expected to magnify for a full-size 1:1 roof component with an aluminum roof panel and steel roof bows. A finite element simulation was performed for a full-size SUV roof component (1900 x 1100 x 1.2mm) with fixations. The FE predictions (shown in Figure 23) showed that the center of the roof component bulged by 35 mm at the peak temperature. This magnitude of displacement will give rise to other practical problems and bonding defects. At this level of bulging, the aluminum panel will not remain in contact with the adhesive applied on the cross-bows and the adhesive will be cured without staying in contact with the two bonding surfaces. Therefore, Z-displacement of such a high order is expected to cause de-bonding in the cross-bows during the curing process of the body structure.

Effect of choice of adhesive: The choice of adhesive can play a role in the optimization of the bonded structure design. Changing the stiffness of the adhesive can help in changing the magnitude of the residual stresses. Figure 24 shows the effects of having a low stiffness adhesive as compared to a high stiffness adhesive.

An adhesive with a lower modulus will have lower residual stresses in the bond due to the manufacturing-induced thermal displacements. It would be beneficial for the adhesive but would have adverse effects on the overall rigidity of the bonded structure. On the other hand, an adhesive with a high modulus will

provide high rigidity to the bonded structure but will give rise to a higher level of manufacturing-induced residual stresses.

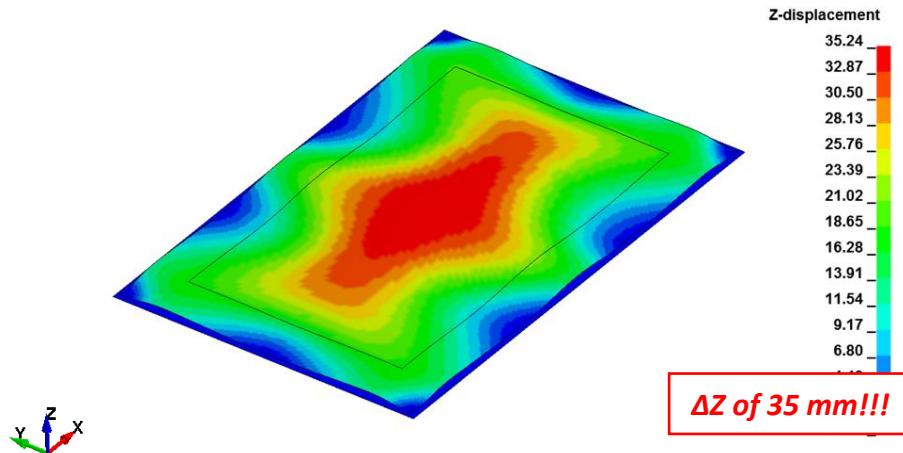


Figure 23. Z-displacement in the aluminum panel for a full size 1:1 roof component with adhesive and mechanical fixations



Figure 24. Effect of the choice of adhesive on the adhesive bond and the body structure stiffness

5. CONCLUDING REMARKS

This paper developed a suite of viscoelastic-plastic models which work in conjunction to predict the manufacturing process-induced effects on an adhesive joint. The models were calibrated for an automotive-grade structural adhesive EP 5089. The material models were coded into a user-defined material subroutine for LS-DYNA. The developed material subroutine was implemented in finite element simulations for performing component level validations on a roof component (a) with adhesive only and (b) with adhesive and mechanical fixations. The predicted results of the finite element simulations showed a match with the experimental results for both scenarios. The developed approach based on only the viscoelastic-plastic modeling of adhesive gives promising results at the component level and sheds light on several important points to consider during the design process.

There are a variety of parameters that play a role in the design process of a lightweight structure: (i) material combination i.e., steel, aluminum, magnesium, or CFRP; (ii) adhesive type i.e. low, medium, or high stiffness adhesive; (iii) bondline geometry i.e. bondline width and adhesive thickness; (iv) curing cycle

(v) fixation design i.e. type, spacing, the number of joints. The discussed problems were not so significant in a steel-intensive structure owing to a low thermal expansion in steel. But these concerns get enlarged in dealing with multi-material structures composed of aluminum or magnesium with a relatively higher coefficient of thermal expansion. The developed package of material models and experiments fills that gap to enable the design of an optimized multi-material lightweight structure by helping in answering the design-related critical questions.

DECLARATION OF COMPETING INTERESTS

The authors declare that they have no known competing financial interests or personal relationships that could have appeared to influence the work reported in this paper.

ACKNOWLEDGEMENTS

The authors would like to thank Henkel Adhesives, North America for funding this study. Special thanks to Dr. Tim Welters and Dr. Georges Romanos from Henkel Corporation, Germany for their technical support.

DATA AVAILABILITY

The raw data required to reproduce these findings are available to download from Mendeley Data. The DSC data for Henkel Teroson EP 5089 is available at [27] , the DMA data for Henkel Teroson EP 5089 is available at [29] , and the temperature-strain dependent uniaxial tension data is available at [30].

APPENDIX

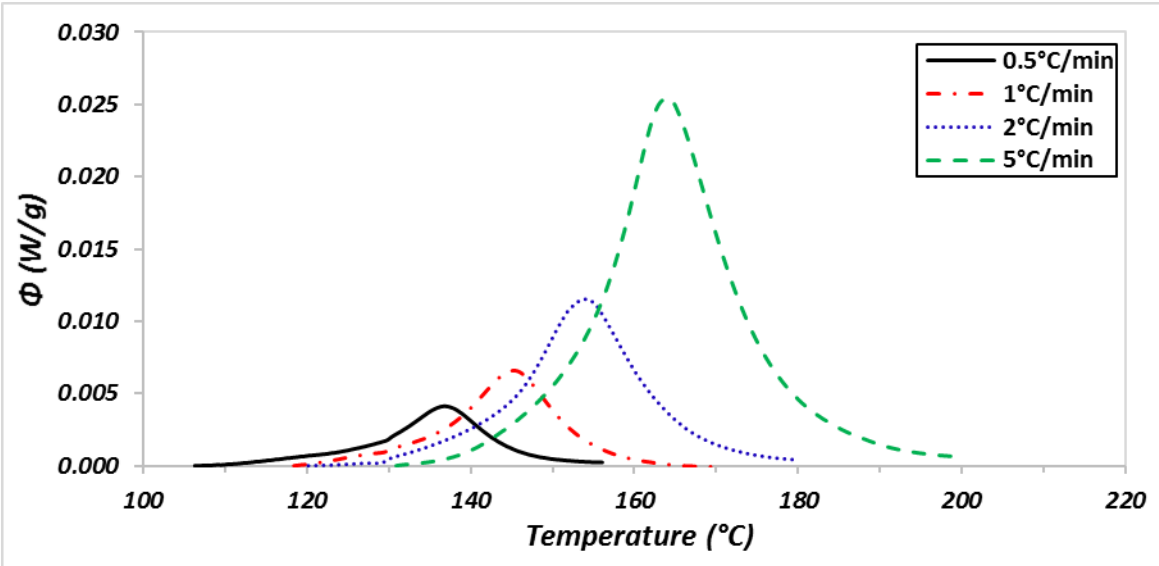


Figure A.1. Sample DSC heat flow scans for EP5089 adhesive normalized with specimen weight for different heating rates [27]

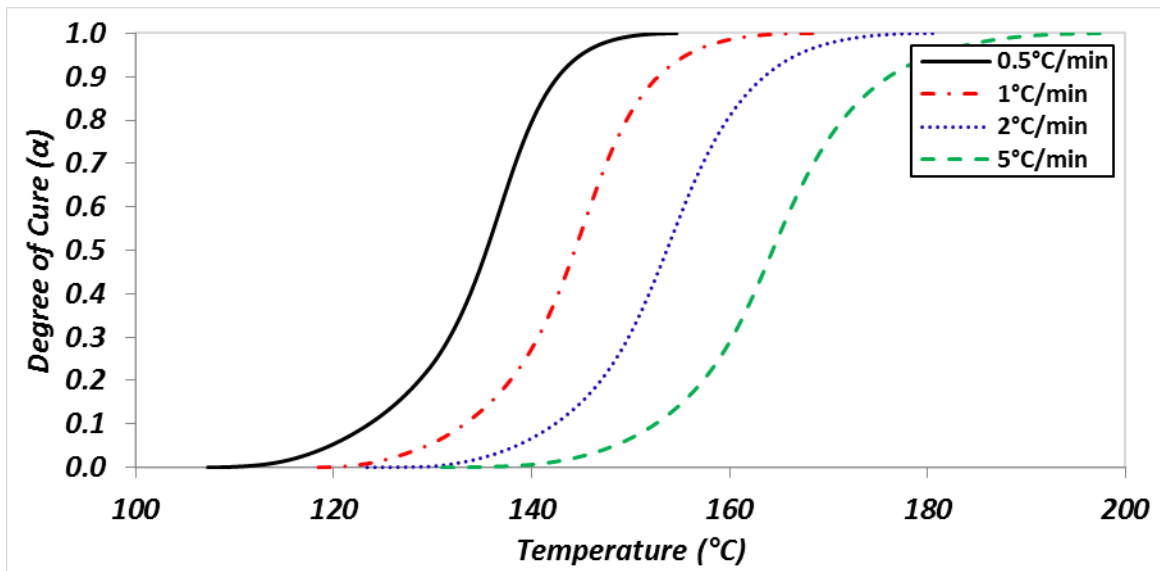


Figure A.2. Degree of cure vs. temperature curves for EP5089 adhesive obtained by integrating the DSC measurement curves at different heating rates

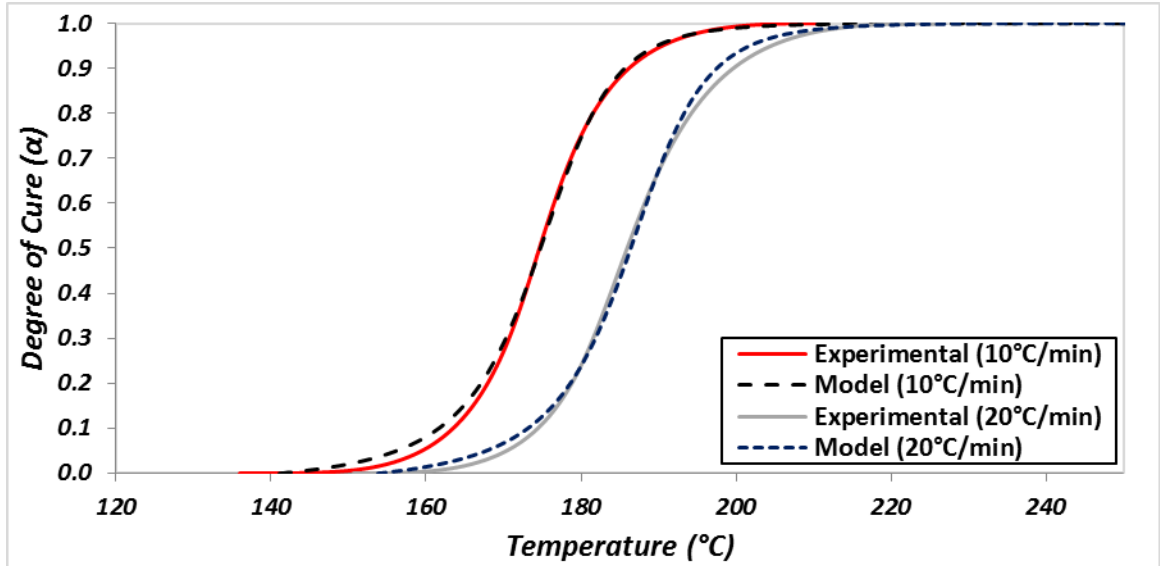


Figure A.3. Comparison of the curing kinetics model prediction and independent experimental curves at non-isothermal conditions

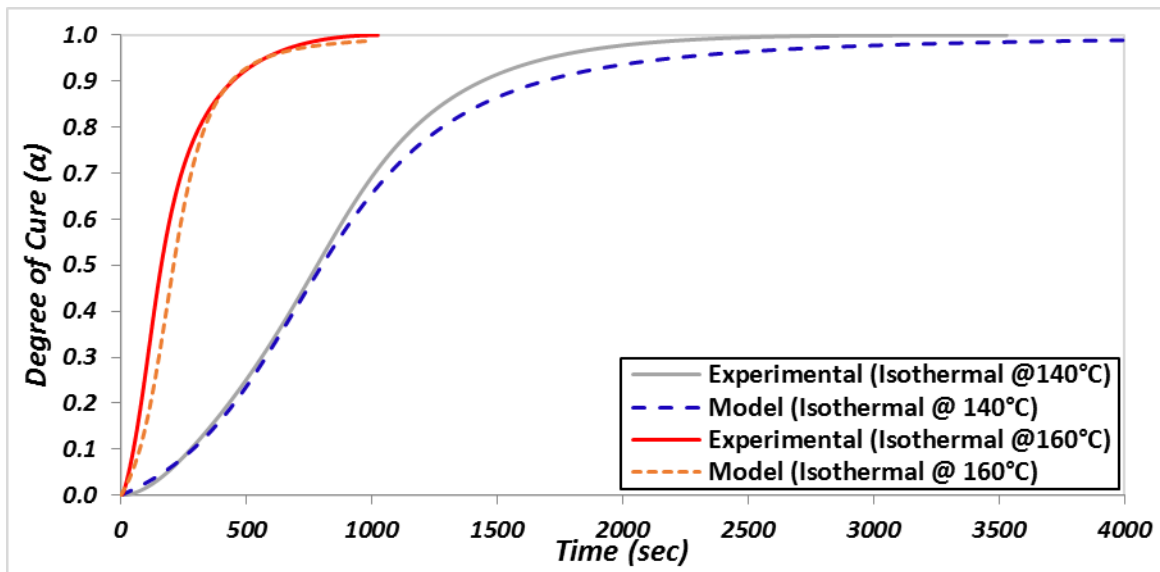


Figure A.4. Comparison of the curing kinetics model prediction and independent experimental curves at isothermal conditions (140°C and 160°C)

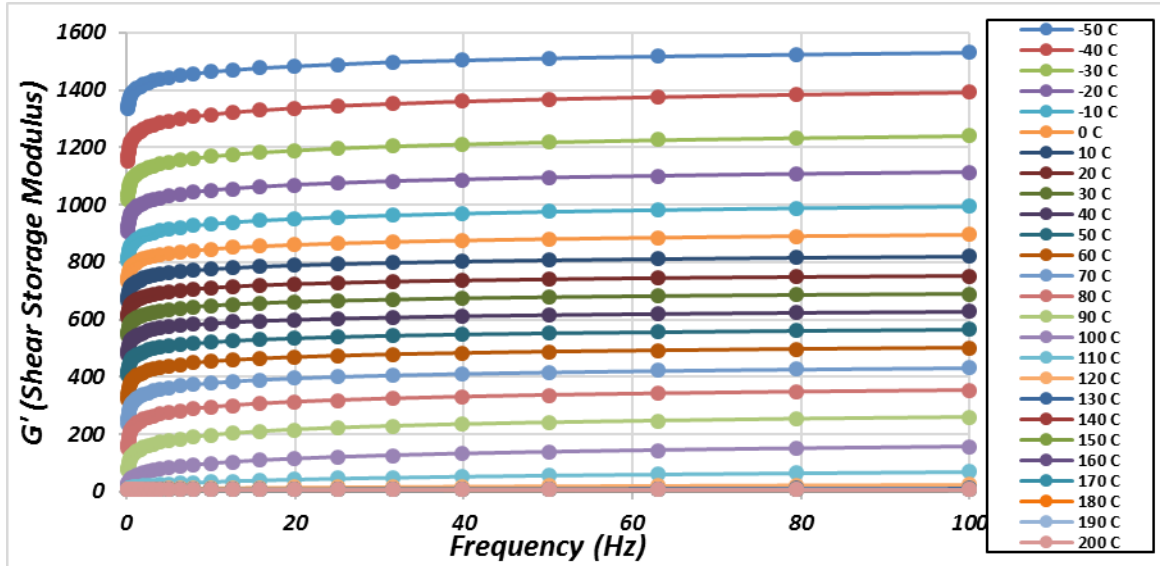


Figure A.5. Shear storage modulus vs. frequency as a result of combined temperature-frequency sweep on DMA tests conducted on EP5089 adhesive [29]

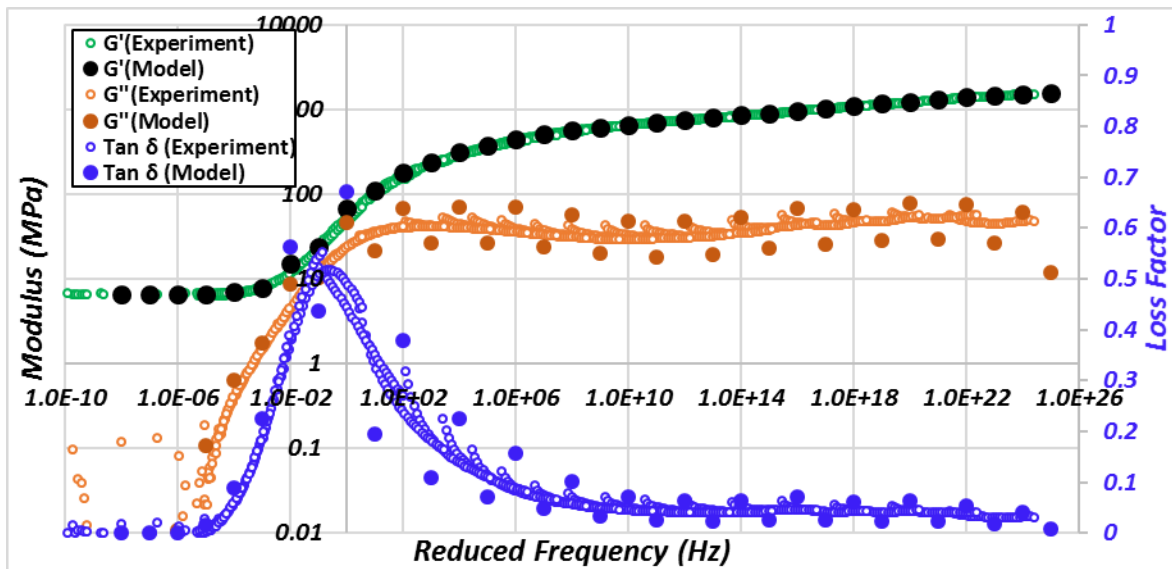


Figure A.6. Master curve showing shear storage, loss modulus and loss factor at 100°C and the Prony series model predictions for EP5089 adhesive

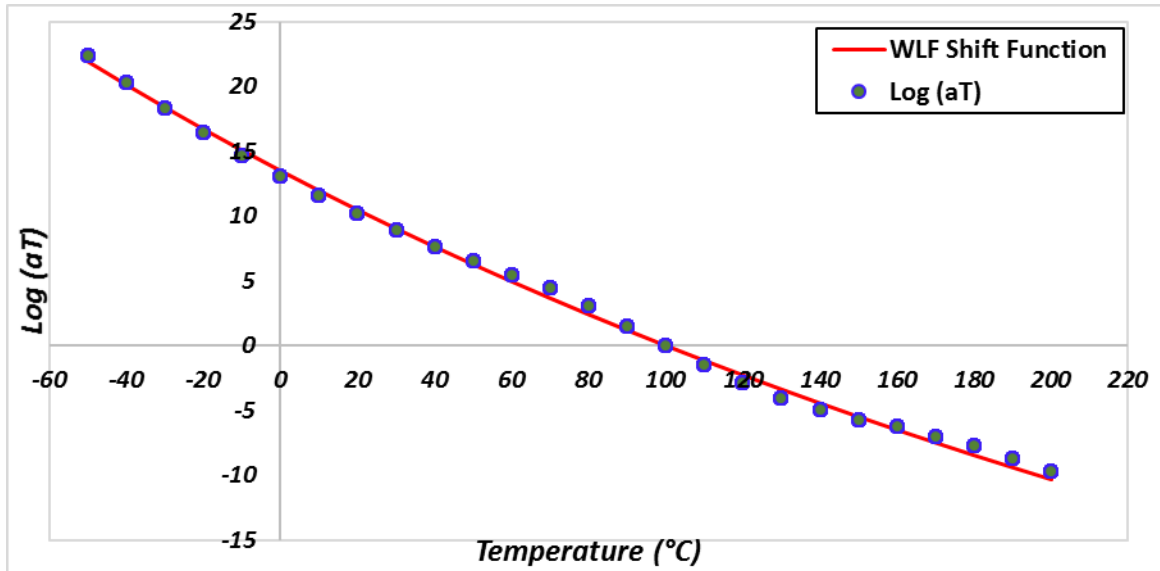


Figure A.7. Comparison of Log of experimental frequency shift factors and WLF model estimation for the master curve at a reference temperature of 100°C for the WLF A' and B' given in Table 2.

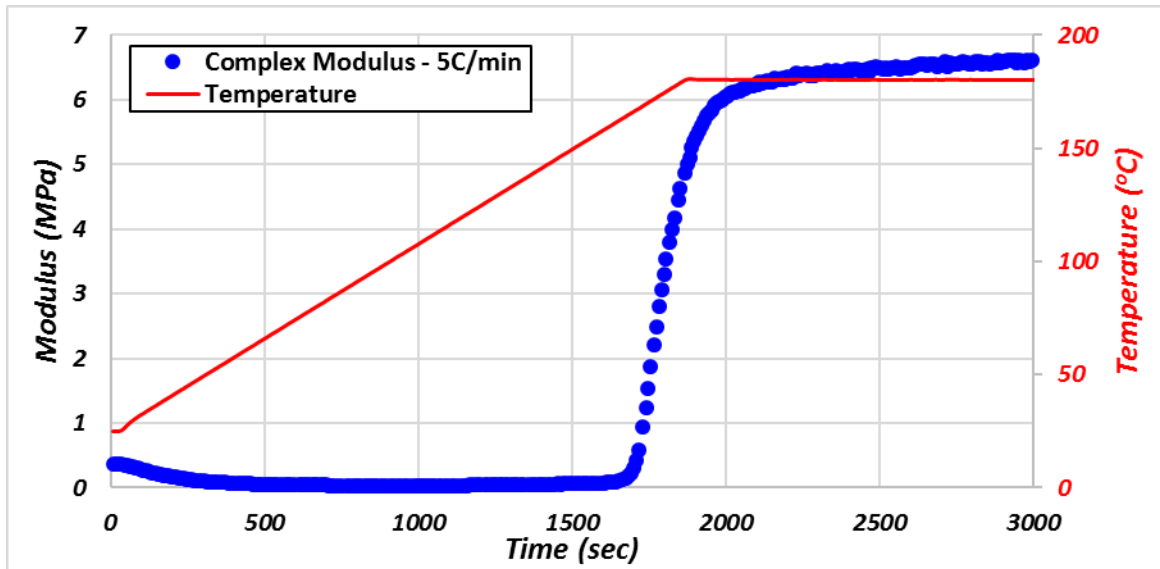


Figure A.8. Development of shear modulus (real part of complex modulus) with time for a temperature ramp of 5°C/min for EP5089 adhesive at a frequency of 100 rad/s

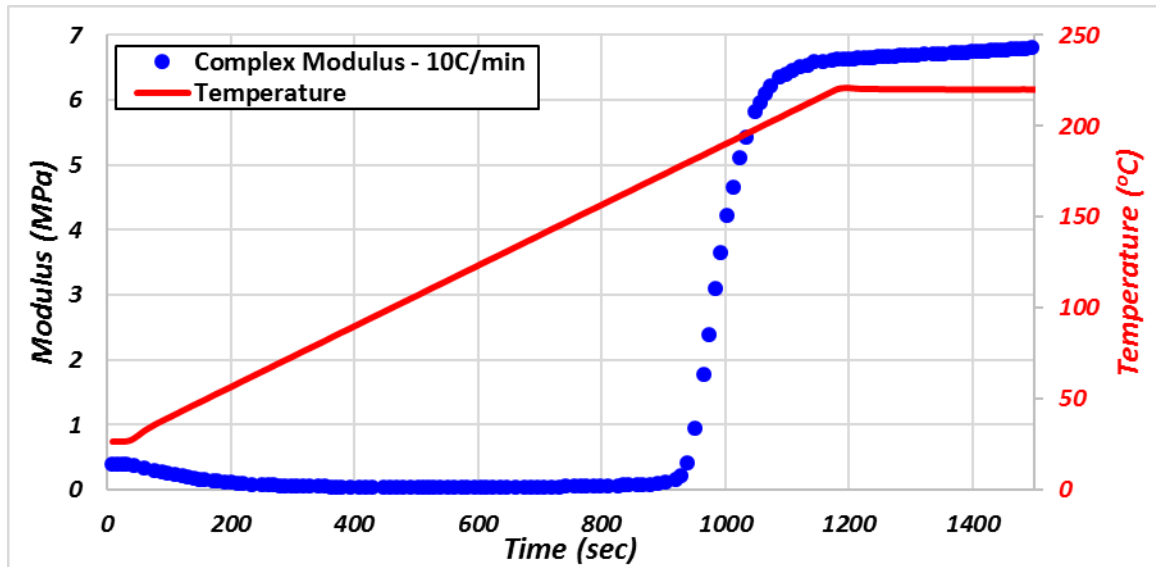


Figure A.9. Development of shear modulus (real part of complex modulus) with time for a temperature ramp of $10^{\circ}\text{C}/\text{min}$ for EP5089 adhesive at a frequency of 100 rad/s

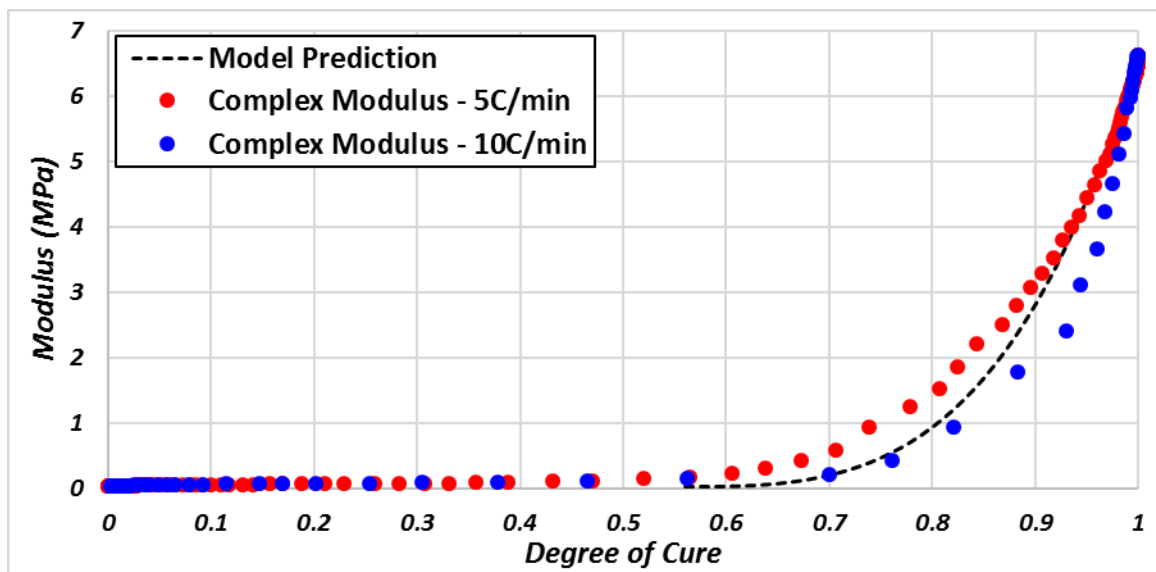


Figure A.10. Comparison of experimentally obtained modulus growth with degree of cure and the numerical model predictions for the EP5089 adhesive

REFERENCES

1. Banea, M.D. and L.F.M. da Silva, *Adhesively bonded joints in composite materials: An overview*. Proceedings of the Institution of Mechanical Engineers, Part L: Journal of Materials: Design and Applications, 2009. **223**(1): p. 1-18.
2. Reedy, E.D. and T.R. Guess, *Butt joint strength: effect of residual stress and stress relaxation*. Journal of Adhesion Science and Technology, 1996. **10**(1): p. 33-45.
3. Agha, A. and F. Abu-Farha, *Experimental methods to capture curing induced effects in adhesive bonded joints*. International Journal of Adhesion and Adhesives, 2021. **104**: p. 102735.

4. Marques, E.A.S., et al., *Adhesive Joints for Low- and High-Temperature Use: An Overview*. The Journal of Adhesion, 2014. **91**(7): p. 556-585.
5. Xiaogang Huang, J.W.G., Travis Bogetti, *Process induced stress for woven fabric thick section composite structures*. Composite Structures, 2000. **49**: p. 303-312.
6. Brauner, C., S. Bauer, and A.S. Herrmann, *Analysing process-induced deformation and stresses using a simulated manufacturing process for composite multispar flaps*. Journal of Composite Materials, 2014. **49**(4): p. 387-402.
7. Ruiz, E. and F. Trochu, *Thermomechanical Properties during Cure of Glass-Polyester RTM Composites: Elastic and Viscoelastic Modeling*. Journal of Composite Materials, 2016. **39**(10): p. 881-916.
8. Li, D., X. Li, and J. Dai, *Process Modelling of Curing Process-Induced Internal Stress and Deformation of Composite Laminate Structure with Elastic and Viscoelastic Models*. Applied Composite Materials, 2017. **25**: p. 527-544.
9. Douglas Adolf, J.E.M., *Calculation of Stresses in Crosslinking Polymers*. Journal of Composite Materials, 1996. **30**(1): p. 13-34.
10. Prasatya, P., G.B. McKenna, and S.L. Simon, *A Viscoelastic Model for Predicting Isotropic Residual Stresses in Thermosetting Materials: Effects of Processing Parameters*. Journal of Composite Materials, 2001. **35**(10): p. 826-848.
11. Courtois, A., et al., *Viscoelastic behavior of an epoxy resin during cure below the glass transition temperature: Characterization and modeling*. Journal of Composite Materials, 2018: p. 002199831878122.
12. da Silva, L.F.M., et al., *Analytical models of adhesively bonded joints—Part II: Comparative study*. International Journal of Adhesion and Adhesives, 2009. **29**(3): p. 331-341.
13. Budhe, S., et al., *An updated review of adhesively bonded joints in composite materials*. International Journal of Adhesion and Adhesives, 2017. **72**: p. 30-42.
14. Agha, A. and F. Abu-Farha, *Viscoelastic model to capture residual stresses in heat cured dissimilar adhesive bonded joints*. International Journal of Adhesion and Adhesives, 2021. **107**: p. 102844.
15. May, M., H. Voß, and S. Hiermaier, *Predictive modeling of damage and failure in adhesively bonded metallic joints using cohesive interface elements*. International Journal of Adhesion and Adhesives, 2014. **49**: p. 7-17.
16. Hu, P., et al., *Strength prediction of adhesively bonded joints under cyclic thermal loading using a cohesive zone model*. International Journal of Adhesion and Adhesives, 2013. **41**: p. 6-15.
17. R.A. Dickie*, D.R.B., S.M. Ward, D.A. Wagner, *Modeling paint and adhesive cure in automotive applications*. Progress in Organic Coatings, 1997. **31 (1997) 209–216**.
18. Zhang, J., Y.C. Xu, and P. Huang, *Effect of cure cycle on curing process and hardness for epoxy resin*. Express Polymer Letters, 2009. **3**(9): p. 534-541.
19. Daoqiang Lu, C.P.W., *Effects of shrinkage on conductivity of isotropic conductive adhesives*. International Journal of Adhesion & Adhesives, 2000. **20 (2000) (20)**: p. 189-193.
20. Kamal, M.R., *Thermoset Characterization for Moldability Analysis*. Polymer Engineering & Science, 1974.
21. Malcolm L. Williams, R.F.L., and John D. Ferry, *The Temperature Dependence of Relaxation Mechanisms in Amorphous Polymers and Other Glass-forming Liquids*. Journal of the American Chemical Society, 1955. **77 (14)**: p. 3701–3707.
22. Meuwissen, M.H.H., et al., *Prediction of mechanical stresses induced by flip-chip underfill encapsulants during cure*. International Journal of Adhesion and Adhesives, 2006. **26**(4): p. 212-225.

23. Hossain, M., G. Possart, and P. Steinmann, *A small-strain model to simulate the curing of thermosets*. Computational Mechanics, 2008. **43**(6): p. 769-779.
24. Kim, Y.K. and S.R. White, *Stress relaxation behavior of 3501-6 epoxy resin during cure*. Polymer Engineering and Science, 1996. **36**: p. 2852-2862.
25. Bogetti, T.A. and J.W. Gillespie, *Process-Induced Stress and Deformation in Thick-Section Thermoset Composite Laminates*. Journal of Composite Materials, 1992. **26**(5): p. 626-660.
26. Johnson, G.R. and W.H. Cook, *Fracture characteristics of three metals subjected to various strains, strain rates, temperatures and pressures*. Engineering Fracture Mechanics, 1985. **21**: p. 31-48.
27. Agha, A., *Differential Scanning Calorimetry (DSC) data for Curing Kinetics Study of thermoset based structural adhesive Henkel Teroson EP5089*. Mendeley Data, 2021. **V1**, doi: **10.17632/tt87pfzkkkg.1**.
28. Agha, A., *Cure Dependent Viscoelastic-Plastic Modeling of Adhesives to Capture CTE Effects in Multi-Material Structures*. All Dissertations, 2019.
29. Agha, A., *Dynamic Mechanical Analysis (DMA) data for thermoset based structural adhesive Henkel Teroson EP5089*. Mendeley Data, 2021. **V1**, doi: **10.17632/k6pggf8zxw.1**.
30. Agha, A., *High-temperature and high strain rates uniaxial tension tests for thermoset based structural adhesive Henkel Teroson EP5089*. Mendeley Data, 2021. **V1**, doi: **10.17632/rrcbysz6b9.1**.
31. Abedrabbo, N., F. Pourboghrat, and J. Carsley, *Forming of aluminum alloys at elevated temperatures – Part 2: Numerical modeling and experimental verification*. International Journal of Plasticity, 2006. **22**(2): p. 342-373.